Atmos. Chem. Phys. Discuss., 15, 4909–4971, 2015
www.atmos-chem-phys-discuss.net/15/4909/2015/
doi:10.5194/acpd-15-4909-2015

Atmospheric Chemistry and Physics Discussions

The impact of observing characteristics on the ability to predict ozone under varying polluted photochemical regimes

P. D. Hamer[1,2], K. W. Bowman[1], D. Henze[3], J.-L. Attié[4], and V. Marécal[2]

[1]Jet Propulsion Laboratory, California Institute of Technology, Pasadena, California, USA
[2]Centre National de Recherches Météorologiques – Groupe d'étude de l'Atmosphère Météorologique, Météo-France and CNRS, UMR3589, Toulouse, France
[3]Department of Mechanical Engineering, University of Colorado, Boulder, Colorado, USA
[4]Laboratoire d'Aérologie, Université de Toulouse, CNRS, UMR, Toulouse, France

Received: 23 December 2014 – Accepted: 3 February 2015 – Published: 23 February 2015

Correspondence to: P. D. Hamer (paul.d.hamer@gmail.com, paul.hamer@meteo.fr)

Published by Copernicus Publications on behalf of the European Geosciences Union.

Abstract

We conduct a variety of analyses to assess how the characteristics of observations of ozone and its precursors affect their ability to support air quality forecasting and research. To carry out this investigation we use a photochemical box model and its adjoint integrated with a Lagrangian 4-D-variational data assimilation system. Using this framework in conjunction with various sets of pseudo observations we perform a ozone precursor source inversion and estimate surface emissions. We then assess the resulting improvement in ozone air quality forecasting and prediction. We use an analytical model as our principle method of conducting uncertainty analyses, which is the primary focus of this work. Using this analytical tool we address some simple but key questions regarding how the characteristics of observations affect our framework's ability to constrain ozone precursor emissions and in turn to predict ozone. These questions include what the effect is of choosing which species to observe, of varying amounts of observation noise, of changing the observing frequency and the observation time during the diurnal cycle, and of how these different scenarios interact with different photochemical regimes. These questions are designed to examine how different types of observing platform, e.g., geostationary satellites or ground monitoring networks, could support future air quality research and forecasting. In our investigation we use three observed species scenarios: CO and NO_2; ozone, CO, and NO_2; and HCHO, CO and NO_2. The photochemical model was setup to simulate a range of summertime polluted environments spanning NO_x (NO and NO_2) limited to volatile organic compound (VOC) limited conditions. We find that as the photochemical regime changes the relative importance of trace gas observations to constrain emission estimates and subsequent ozone forecasts varies. For example, adding ozone observations to an NO_2 and CO observing system is found to decrease ozone prediction error under NO_x and VOC limited regimes, and complementing the NO_2 and CO system with HCHO observations would improve ozone prediction in the transitional regime and under VOC limited conditions. We found that scenarios observing ozone and HCHO with relative observing

ACPD
15, 4909–4971, 2015

noise of lower than 33 % were able to achieve ozone prediction errors of lower than 5 ppbv (parts per billion by volume). Further, only observing intervals of 3 h or shorter were able to consistently achieve ozone prediction errors of 5 ppbv or lower across all photochemical regimes. Making observations closer to the prediction period and either in the morning or afternoon rush hour periods made greater improvements for ozone prediction. Finally, we made two complimentary analyses that establish the robustness of our conclusions to the assumed diurnal emission cycle and to the choice of which VOC species emission to estimate using our framework.

1 Introduction

Ozone is a hazard to human health, plants and animals and a greenhouse gas (Mustafa, 1990; Pryor, 1992; Murphy et al., 1999; Fumagalli et al., 2001; Nali et al., 2002; IPCC, 2007; Van Dingenen et al., 2009; WHO, 2013). Prediction of ozone air quality on local and regional scales is key for providing prior warning of impending ozone exceedances (Dabberdt et al., 2004, 2006). Knowledge of the processes that control the variability of ozone precursors is vital for understanding and predicting ozone air quality.

Currently, a wide variety of techniques are used to predict ozone concentrations ranging from statistically based models (Gardner and Dorling, 2000), neural networks (Yi and Prybutok, 1996), to prognostic models of atmospheric processes that include data assimilation (Grell et al., 2005; Otte et al., 2005; Zhang et al., 2008; Kang et al., 2010). For prognostic models, uncertainties result from meteorology, the limitations of the photochemical mechanisms, wet and dry deposition, uncertainties in the emissions of ozone precursors, and, for data assimilation, observation uncertainty (Dabberdt et al., 2004, 2006). Most current statistical and data assimilation air quality forecasting techniques rely primarily on surface observing networks, but satellite observations are increasingly coming to the fore.

ACPD
15, 4909–4971, 2015

Ozone pollution can develop under different polluted photochemical regimes. Under low to moderate levels of NO_x (NO and NO_2) pollution, such as can be found in rural and suburban environments, increases in NO_x lead to proportional increases in ozone, which is why this regime is classed as NO_x-limited (Trainer et al., 1987; Sillman, 1993; Jacob et al., 1993). Under much higher levels of NO_x pollution, i.e., those present in densely populated regions, increases in NO_x actually bring about decreases in ozone. Under these conditions, the only means by which ground level ozone can increase are via increases in VOC emissions (Finlayson-Pitts and Pitts, 1997), and consequently this regime is considered to be VOC-limited. Further, studies show that the sensitivity of ozone to either NO_x or VOCs can vary with time, e.g., during different days of the week (Blanchard and Fairley, 2001; Blanchard and Tanenbaum, 2003). The priorities to monitor and observe ozone and its different precursors therefore vary according to location and time.

Observations and models, and their combination through data assimilation, comprise essential tools for air quality prediction (Zhang et al., 2008; Strunk et al., 2010; Zhang et al., 2012). Observations are an essential part of such systems, so it follows that their characteristics could directly affect their performance. We seek to address this connection in our study. Given this, we will now attempt to review the relevant characteristics of the current and planned (in the near term) state of the air quality monitoring network in order to motivate our work and, later, to place some of our findings in context.

The US national surface air quality observing network typically observes a wide range of chemical species. For instance, surface monitoring sites within California (http://www.arb.ca.gov/adam/) have instruments that can measure in-situ ozone, CO, NO_2, nitrogen oxide, particulate matter with diameters of 2.5 and 10 µm, sulphur dioxide (SO_2), methane, total hydrocarbons, and hydrogen sulphide. The surface network is also usually able to make observations at least at hourly temporal resolution. However, due to the spatial limitations of the surface air quality monitoring network, space-borne remote sensing observations, which typically have greater spatial sampling, are also

ACPD
15, 4909–4971, 2015

able to support air quality research and later operational air quality forecasting (Lahoz et al., 2012).

For this study, the spatial characteristics of observations from different platforms are not considered, but the advantages satellite data offer in terms of increased spatial coverage have been recognised and should be noted. Consequently, various studies have been conducted that highlight the benefits of satellite borne instruments for air quality research (Martin, 2008; Duncan et al., 2010; Jones et al., 2009; Bowman et al., 2009; Kurokawa et al., 2009; Konovalov et al., 2006; Millet et al., 2008; Kopacz et al., 2010; Arellano et al., 2006; Dufour et al., 2010; Fishman et al., 2010). Further, satellite observations of air pollutants have been used within data assimilation models to advance air quality research (Sandu et al., 2003a; Chai et al., 2007; Pierce et al., 2007; Zhang et al., 2008; Parrington et al., 2009).

Excluding the issue of spatial sampling, there are considerable differences between remote sensing observations and the existing surface observing network. Each individual ground station is able to observe a wider range of species at the surface (see above) but only at a single point. On the other hand, space-based remote sensing techniques can only observe a limited number of species that have relevance to air quality (such as ozone, CO, NO_2, SO_2, CH_4, glyoxal, and HCHO), have coarser horizontal spatial resolution observing with a footprint ranging from several to up to tens of kilometers, and have (with current capabilities) only limited vertical resolution and sensitivity to the surface or boundary layer. Also, all of the studies cited above used instruments onboard satellites in low earth orbit (LEO). Due to the orbital configuration, LEO borne instruments are only able to observe the same location on a far more infrequent basis compared to the temporal sampling of the ground based network.

Instruments onboard geostationary (GEO) satellites can also offer good spatial coverage (at the continental and regional scale) without sacrificing temporal sampling. This makes them potentially ideal to support future air quality research and forecasting. However, in order to achieve this goal, developments must be made to improve satellite instrument sensitivity to the boundary layer and surface gas phase composition (Lahoz

ACPD
15, 4909–4971, 2015

et al., 2012). Various strategies have been proposed to achieve this aim (primarily for CO and ozone). They typically consist of either combining wavelength bands that have been previously exploited, i.e., UV, visible, and IR (Landgraf and Hasekamp, 2007; Worden et al., 2007, 2010), or by focusing on new wavelength bands, i.e., the Chappuis bands for ozone in the visible (Zoogman et al., 2011) that offer potential novel benefits. The UV and Chappuis band in the visible were combined theoretically to determine the benefit of such an approach during the development of the TEMPO instrument (Zoogman et al., 2014) and as part of an European intiative (Hache et al., 2014).

As a result of the perceived benefits, several GEO missions are currently in the various stages of planning. These include the Geostationary Coastal and Air Pollution Events (GEO-CAPE) planned by NASA to cover the North American continent (http://science.nasa.gov/earth-science/decadal-surveys/). Sentinel 4 (http://www.esa.int/esaLP/SEM3ZT4KXMF_LPgmes_0.html) is planned by ESA to cover Europe, and the Geostationary Environment Spectrometer (GEMS) (Lee et al., 2009) is aimed at providing coverage of East Asia. Further, NASA's decadal survey and Lee et al. (2009) indicate that GEO-CAPE and GEMS will observe the following trace gases: ozone, CO (not with GEMS), NO_2, HCHO, and SO_2.

GEO based observations of trace gases are therefore becoming more relevant for the study of air quality and for operational air quality forecasting. For the planned GEO missions, various choices exist regarding which wavelength bands to observe in, and these will influence the already limited range of observable species in the troposphere. In addition, instrument design choices affect how often observations can be made, at what time of day, and how well. For instance, thermal infrared (TIR) based instruments can not measure NO_2, and UV-VIS instruments can not observe during the night time. Thus, instrument design choices will affect the future capabilities of these missions.

We have demonstrated that a range of possible capabilities and characteristics exist for both the current and planned air quality observing systems (ground and satellite based). Within the scope of this paper, we study how the frequency and specific timing during the day of observation, the species that get measured, and how well they get

ACPD
15, 4909–4971, 2015

measured affect the ability to conduct air quality research and to aid air quality forecasting using a data assimilation system. This interaction between observation characteristics and data assimilation system performance remains an open question in this context. Therefore, addressing this question will be of interest to the current air quality observing network and to the planned or future GEO air quality focused missions. In order to do this we carry out a series of sensitvity analyses using different sets of simplistic pseudo observations to test the influence various observation characteristics have upon the ability to predict ozone within an idealised model. This model consists of a photochemical box model, its adjoint, and a 4-D-variational data assimilation system setup to constrain ozone pre-cursor emission uncertainties (NO_x, CO, and VOCs). This framework thereby mimics a state of the art air quality forecasting system. We conduct an uncertainty analysis using a linear estimation technique for each of our sensitivity tests. We are able to perform the uncertainty analysis owing to the fact that we use a box model because it limits the size of the matrices we solve for. Within the context of a summertime ozone pollution episode that emerges during stagnant anticyclonic conditions we attempt to address the following specific aims:

- How does the ability to predict ozone vary across three separate observing scenarios? The first uses only CO and NO_2 observations (CN), the second uses Ozone, CO, and NO_2 (OCN), and the third uses HCHO, CO, and NO_2 (HCN).
- What are the effects of both observing frequency and the choice of when to observe on the prediction of ozone within our framework?
- How does observation noise, when applied evenly onto each observation, affect ozone prediction in our system?
- How are the results of these sensitivity tests affected by photochemical regime? I.e., either NO_x or VOC limited.
- Ignoring ozone prediction, which combination of observed species allows the best constraint on ozone precursor emissions?

ACPD
15, 4909–4971, 2015

In order to support our conclusions regarding the aims above we carry out a variety of complementary analyses:

- To demonstrate that the 4-D-variational data assimilation scheme can solve the full non-linear retrieval of the emission parameters.
- To test the robustness of our methodology to choices regarding our assumed diurnal emission profile.
- To test whether the assumed VOC emission uncertainties can be represented using different VOCs.

Section 2 describes all aspects of the methodology, Sect. 3 describes the results from each of the analyses, Sect. 4 discusses our results, Sect. 5 details our conclusions.

2 Methodology

2.1 Overview

We use a photochemical box model run over 3 days to represent a worsening period of ozone air quality during a stagnation event. Meteorological stagnation events under hot, sunlit conditions over urban areas typically lead to poor ozone air quality (Jacob et al., 1993; Valente et al., 1998). We assume that the idealised mixing and transport represented in the box model are sufficient to represent the meteorology during anti-cyclonic conditions. For each of the different sensitivity tests that we perform we use different sets of pseudo observations of ozone, HCHO, CO and NO_2 (see Sect. 2.3, and examine Fig. 3 to see an example of the pseudo observations relative to the true ozone state) in order to separately constrain the ozone precursor emissions with the 4-D-variational data assimilation system. The ozone percursor emissions have known a priori errors. We then make a prediction of ozone using the a posteriori emissions. Within the model framework, days 1–2 represent the period over which observations

ACPD
15, 4909–4971, 2015

are made and the assimilation is carried out and the final day represents the prediction and monitoring period. Within this final phase, we compare the ozone prediction, based upon the a posteriori emissions, to the ozone true state in order to assess the assimilation performance. We support this assessment using a range of statistics and diagnostics that shall be discussed shortly.

The use of 4-D-variational data assimilation to solve the ozone precursor emission inversion problem is consistent with the current state of the art in prognostic air quality forecast modeling development. For example, the Community Multi Scale Air Quality Modeling System, Hakami et al. (2007) and the Sulfur Transport Eulerian Model, Zhang et al. (2008), and Elbern et al. (2007) are all developing such assimilation capabilities. Thus, our model framework is relevant to and is reflective of the current and future direction of air quality forecasting.

In order to establish the utility of more complex air quality forecasting systems that might use 4-D-variational data assimilation, our prototype forecasting system is demonstrated theoretically. Since the emission inversion problem that we explore only becomes more complex as the model state space increases and additional sources of uncertainty are introduced, a failure to show sufficiently reduced prediction error in this simplified setting would indicate that more complex systems are unlikely to fare better. Sufficient prediction model error within our framework is therefore a necessary but not sufficient condition for more complex 4-D-variational data assimilation forecasting systems using air quality observations to be successful.

One other advantage of selecting a photochemical box model is that we are able to generate a Jacobian describing the model response to emission parameter perturbations, which can be used within an analytical modeling framework to conduct uncertainty analysis. It would be very difficult to produce a Jacobian within a regional or global chemical transport models in a timely fashion given the size of the model state space. Therefore we use an analytic model (derived from the photochemical box model) that is simplified relative to the full assimilation framework. This is a linear estimation technique based upon Rodgers (2000). To support our analyses we calculate

ACPD
15, 4909–4971, 2015

the following diagnostics using this method: a posteriori ozone prediction error covariance, a posteriori emission parameter error covariance, the averaging kernel, and the degrees of freedom of signal.

The 4-D-variational data assimilation and uncertainty analysis using the linear estimation are therefore complementary methods, and we use both techniques to achieve our aim of exploring the effect of observing characteristics on ozone prediction.

In addition, we conduct a series of supporting analyses. Since we assume a fixed diurnal variability of ozone precursor emissions, we study the impact on our conclusions of changing the diurnal variability of emissions. When conducting the VOC emission inversion we solve ethene emission uncertainties (rather than a more diverse range of VOCs) we therefore test that assumption in a sensitivity analysis by assuming VOC emission errors for ethane instead of ethene.

2.2 Photochemical box model

A 1-dimensional photochemical box model was built using the Kinetic Pre-Processor (KPP) (Damian et al., 2002; Daescu et al., 2003; Sandu et al., 2003b). The Rosenbrock solver is used to integrate the KPP generated ordinary differential equations required to calculate trace gas concentrations (Eller et al., 2009). The photochemical mechanism consists of 171 gas phase species and 524 chemical reactions simulating the degradation of hydrocarbons from C_1–C_5 including isoprene and is based upon the Master Chemical Mechanism v3.1 (Jenkin et al., 1997) (http://mcm.leeds.ac.uk/MCM/). In addition, the model includes dry deposition for all relevant chemical species, it contains a 2-parameter photolysis scheme, and it simulates the emission of ozone precursors including NO_x, CO, and volatile organic compounds (VOCs). The diurnal emission variability of anthropogenic compounds is prescribed according to the National Atmospheric Emissions Inventory (NAEI) (http://www.naei.org.uk/emissions/) for an urbanised area (see Fig. 1), and the isoprene emission variability is parameterized to correlate to solar zenith angle offset by 2 h to consider both temperature and photon flux effects (Tingey et al., 1979; Tawfik et al., 2012). The isoprene emissions have

ACPD
15, 4909–4971, 2015

an average daily emission of 1.7×10^{10} molecules $m^{-2}\,s^{-1}$ and an afternoon peak of 4.6×10^{10} molecules $m^{-2}\,s^{-1}$, which yields modeled isoprene mixing ratios less than 10 pptv (parts per trillion by volume). The diurnal variability of the isoprene emissions is separate and distinct to the anthropogenic VOCs. From now on, when we discuss VOCs we are referring to anthropogenic VOCs unless otherwise stated. The VOC speciation is defined according to NAEI and the total peak emission of carbon via VOCs (excluding isoprene) is 2.3×10^{12} carbonatoms $m^{-2}\,s^{-1}$ and the average emission is 1.2×10^{12} carbonatoms $m^{-2}\,s^{-1}$. Boundary layer dynamics are described with a prescribed variability in mixing height ranging from 500–1500 m and mixing between the boundary layer and free troposphere equivalent to a constant 10 % mass exchange per hour. Background free tropospheric concentrations of long lived species are assumed to remain constant, and are defined in Table 1. The box model is situated at 33° North and is run from 30 June to 2 July and has a humidity of 1.62 %, equivalent to the Southern Californian coastal region.

The model is run under a range of photochemical conditions. This is achieved by varying the NO emissions across 9 different scenarios that span the full range of modeled ozone response with respect to changing NO_x concentration (i.e., from NO_x to VOC limited conditions). For the purposes of the emission inversion we define our ozone precursor emissions in a simplified form (excluding emitted species not considered in the inversion) as

$$\phi_i(t) = x_i E_i(t),\ i = \mathrm{NO, CO, VOC} \tag{1}$$

where x_i are the time independent emission scaling factors for the emitted species, i, and $E_i(t)$ are the emissions with a prescribed and repeating diurnal cycle for each emitted species. The emission inversion solves for, x_i, the time independent emission scaling factors, which can be represented as a vector, $\boldsymbol{x}$, for the emitted species, i, as shown by

$$[\boldsymbol{x}]_i = x_i\ ,\ i = \mathrm{NO, CO, VOC} \tag{2}$$

ACPD
15, 4909–4971, 2015

Further, we define the true state of the emission scaling factors as $\boldsymbol{x}t$. The variability of $E_{NO}(t)$ is shown in Fig. 2 and this variability is represented by

$$E_i(t) = e_i k(t) \quad (3)$$

where $k(t)$ is the temporal variability emission factor for all of the emitted species and e_i is the time independent emission for each species. Note then that all of the anthropogenic emissions (NO, CO, and VOCs), $E_i(t)$, share the same temporal variability. The variability of $k(t)$ is shown in Fig. 1. In our model simulations e_{NO} is 4.8×10^{10} molecules $m^{-2}\,s^{-1}$, e_{CO} is 2.6×10^{12} molecules $m^{-2}\,s^{-1}$, and e_{VOC} is 4.3×10^{10} molecules $m^{-2}\,s^{-1}$ where in the emission inversion calculations we represent VOC emissions via ethene emissions. We define a range of different $k(t)$ scenarios in order to probe the emission solution sensitivity to diurnal emission variability and these along with the true variability are shown in Fig. 1.

In the emission inversion calculations we represent VOC emissions via ethene emissions. We selected ethene because it is a sufficiently reactive gas that is emitted in abundance through the course of anthropogenic activity. Thus, the adjoint sensitivities to ethene emissions allowed the proper functioning of the 4-D-var system. $\overline{k(t)}$ is 1.89 (note, overbar indicates the mean value of a variable here and elsewhere), and therefore the average emissions are a factor of 1.89 larger than e_i. In the case of NO, $\overline{E(t)}_{NO}$ is 9×10^{10} molecules $m^{-2}\,s^{-1}$. The scalings used x_{NO} = [0.5, 0.75, 1.0, 1.25, 1.5, 1.75, 2.0, 2.25, and 2.5] lead to a range in $\overline{E(t)}_{NO}$ between 4.5×10^{10} and 2.3×10^{11} molecules $m^{-2}\,s^{-1}$, and to modeled peak NO_x concentrations ranging between 4.0 and 24.0 ppbv (peak concentrations from 1 to 11.3 ppbv for NO and 3 to 16.9 ppbv for NO_2). These NO emission scalings are chosen to represent a wide range of photochemical conditions and given the VOC burden in the model, x_{NO} scalings 0.5, 0.75 and 1.0 represent NO_x limited conditions, 1.25, 1.5 and 1.75 represent transitional conditions, and 2.0, 2.25, and 2.5 represent VOC limited conditions. $\overline{E(t)}_{CO}$ is 5×10^{12} molecules $m^{-2}\,s^{-1}$ and $\overline{E(t)}_{VOC}$ (for ethene) 8.2×10^{10} molecules $m^{-2}\,s^{-1}$. Given

ACPD
15, 4909–4971, 2015

the latitude, humidity, dominance of the VOC burden from anthropogenic VOCs, and range of modeled NO_x concentrations these model runs can be viewed as somewhat analogous to a range of environments spanning the wider urbanized Southern Californian region. The emissions of CO and VOCs lead to modeled peak concentrations of CO and HCHO ranging between 590 and 820 and 6.5 and 8.1 ppbv, respectively.

2.3 Forecasting framework and 4-D-variational data assimilation

Several NO_x emissions scenarios are simulated to cover a wide range of photochemical conditions (x_{NO} = 0.5–2.5). Each emission scenario is represented mathematically as a forward model, $\boldsymbol{F}(\boldsymbol{x},t)$, which are the concentrations as a function of time evaluated at emissions $\boldsymbol{x}$. Depending on the scenario, either pseudo observations of CO, NO_2, O_3, or HCHO are used in various combinations (see Fig. 3 for a representation of the ozone pseudo observations relative to the true state for ozone). In order to derive the pseudo observations the model true state is sampled at 3 hourly intervals in the standard scenarios (used as default unless specified) and at intervals between 1 and 24 h in scenarios characterizing the impact of observing frequency on prediction error. The sampled species concentrations are then combined with an additive noise model to generate the pseudo observations, $\boldsymbol{y}$, represented by

$$\boldsymbol{y} = \boldsymbol{F}(\boldsymbol{x},t) + \boldsymbol{n} \tag{4}$$

where $\boldsymbol{n}$ is the noise

$$\boldsymbol{n} = \overline{\boldsymbol{F}(\boldsymbol{x})} \times \beta \times \epsilon \tag{5}$$

and where $\overline{\boldsymbol{F}(\boldsymbol{x})}$ is the average species concentration (values shown in Table 2), β is the noise scaling factor, and ϵ is a random number with a gaussian distribution, a SD of 1, and a mean of zero. The modeled concentrations for all species and times resulting from $\boldsymbol{F}(x)$ can be represented as a vector, $\boldsymbol{q}$,

$$\boldsymbol{q} = \boldsymbol{F}(\boldsymbol{x},t) \tag{6}$$

ACPD
15, 4909–4971, 2015

or for specific species, z, at time, t, as $\boldsymbol{q}_{z(\boldsymbol{x},t)}$,

$$\boldsymbol{q}_z(\boldsymbol{x},t) = [\boldsymbol{F}(\boldsymbol{x},t)]_z \tag{7}$$

where z can be O_3, NO_2, CO or HCHO. We define a priori emission scaling factors, $\boldsymbol{x}_a$, with specified errors relative to $\boldsymbol{x}t$ (Table 3 provides a summary of the values of x used for both $\boldsymbol{x}t$ and $\boldsymbol{x}_a$), which are combined with the model to yield the a priori model state, $\boldsymbol{F}(\boldsymbol{x}_a)$. Note that within our framework the a priori is also the initial guess.

The assimilation is started at the first iteration with the forward model using the initial guess and is thus described as $\boldsymbol{F}(\boldsymbol{x}_a)$ after one iteration. A cost function, which is a scalar, $J(\boldsymbol{x})$, is then evaluated

$$J(\boldsymbol{x}) = \frac{1}{2}\left((\boldsymbol{y}-\boldsymbol{F}(\boldsymbol{x}))^{\mathrm{T}}\mathbf{S}_n^{-1}(\boldsymbol{y}-\boldsymbol{F}(\boldsymbol{x})) + \frac{1}{2}(\boldsymbol{x}-\boldsymbol{x}_a)^{\mathrm{T}}\mathbf{S}_a^{-1}(\boldsymbol{x}-\boldsymbol{x}_a)\right) \tag{8}$$

where $\mathbf{S}_a$ is the a priori constraint matrix and $\mathbf{S}_n$ is the observation error covariance. The 4-D-variational data assimilation method seeks the solution for $\boldsymbol{x}$, $\hat{\boldsymbol{x}}$, that minimizes $J(\boldsymbol{x})$

$$\hat{\boldsymbol{x}} = \min_{\boldsymbol{x}} J(\boldsymbol{x}) \tag{9}$$

such that the gradient of the cost function with respect to $\boldsymbol{x}$ is zero if the solution $\hat{\boldsymbol{x}}$ is equal to the true state, $\boldsymbol{x}t$, (though this is never fully achieved)

$$\nabla_{\boldsymbol{x}} J = \mathbf{K}^{\mathrm{T}}\mathbf{S}_n(\boldsymbol{y}-\boldsymbol{F}(\hat{\boldsymbol{x}})) - \mathbf{S}_a^{-1}(\hat{\boldsymbol{x}}-\boldsymbol{x}_a) = 0 \tag{10}$$

where $\mathbf{K}$ is the Jacobian matrix (see Eq. 15) describing the forward model response to perturbations to the emission parameters, and $\nabla_{\boldsymbol{x}^t} J$ is the adjoint sensitivity (Daescu et al., 2003; Sandu et al., 2003b), calculated by the Rosenbrock solver (Eller et al., 2009), which indicates the sensitivity of the cost function to the emission parameters. The cost function and its adjoint sensitivities are passed to the quasi-Newton L-BFGS algorithm (Zhu et al., 1997). The L-BFGS algorithm iteratively determines the optimal

ACPD
15, 4909–4971, 2015

state of $\boldsymbol{x}$, $\hat{\boldsymbol{x}}$, that minimizes the difference between the model and observations subject to the a priori constraints.

Using the estimated emissions, $\hat{\boldsymbol{x}}$, the forward model, $\boldsymbol{F}(\hat{\boldsymbol{x}})$, provides the air quality prediction of the ozone concentration, $q_{O_3}(\boldsymbol{x},t)$, on the afternoon of the 3rd day of the simulation during the prediction and monitoring period. The relevance of $q_{O_3}(\boldsymbol{x},t)$ to the prediction and monitoring period is shown in Fig. 3.

Figure 2 shows how the a priori emissions, $\boldsymbol{x}_a$, relate to the true emissions $\boldsymbol{x}$, and the a posteriori emissions, $\hat{\boldsymbol{x}}$, after the 4-D-variational data assimilation, as well as the a priori, the true and the a posteriori ozone levels (i.e., $q_{O_3}(\boldsymbol{x}_a,t)$, $q_{O_3}(\boldsymbol{x},t)$, and $q_{O_3}(\hat{\boldsymbol{x}},t)$, respectively). Figure 2 therefore demonstrates the mechanism by which the forecasting framework improves the forward model ozone predictions, i.e., by an optimization of the ozone precursor emissions. The left panel of Fig. 2 shows the a priori emission error for NO emissions and the right panel shows the a posteriori NO emission error. The a posteriori emission parameter error can be defined more generally as a vector $\widetilde{\boldsymbol{x}}$.

$$\widetilde{\boldsymbol{x}} = \hat{\boldsymbol{x}} - \boldsymbol{x}t \tag{11}$$

Figure 3 provides an example representation of the pseudo observations, ozone prediction, $q_{O_3}(\hat{\boldsymbol{x}},t)$, relative to the true state, $q_{O_3}(\boldsymbol{x},t)$, during the prediction and monitoring period on the third day. In Fig. 3 E represents the a posteriori ozone prediction error at time, t^{μ} (t^{μ} is 3 p.m. on day 3 during the prediction and monitoring period), defined by

$$E = q_{O_3}(\hat{\boldsymbol{x}},t^{\mu}) - q_{O_3}(\boldsymbol{x},t^{\mu}) \tag{12}$$

In Fig. 3 G represents the a priori ozone prediction error defined by

$$G = q_{O_3}(\boldsymbol{x}_a,t^{\mu}) - q_{O_3}(\boldsymbol{x},t^{\mu}) \tag{13}$$

The air quality prediction error over the entire prediction and monitoring period for each of the species, z, can be defined as a vector, $\widetilde{\boldsymbol{q}}$

$$\left[\widetilde{\boldsymbol{q}}_z\right]_j = q_z(\hat{\boldsymbol{x}},t_j) - q_z(\boldsymbol{x},t_j)\ ,j = 3,6\ldots21,24 \tag{14}$$

ACPD
15, 4909–4971, 2015

where j is the hour of day on the 3rd day during the prediction and monitoring period.

2.4 Uncertainty analysis

2.4.1 Overview

The uncertainty analysis has two separate foci: the estimation of the performance of the emissions and an estimation of the a posteriori ozone prediction error. Note that there is a direct synergy between these two analyses since uncertainties in the emissions estimate directly impact upon ozone prediction uncertainty. The diagnostics that we calculate in the analysis of the emissions uncertainties include the a posteriori emission parameter error, the averaging kernel matrix, and the degrees of freedom of signal.

2.4.2 The Jacobian matrix

The Jacobian matrix is redundant within 4-D-variational data assimilation, but it can help characterize the uncertainties on $\widetilde{\boldsymbol{x}}$ and $\widetilde{\boldsymbol{q}}$. Therefore it is advantageous to determine **K**. Within our framework we define each element of **K** as the forward model response, $\partial q_z(\boldsymbol{x},t)/\partial x_i$, at time, t, and for observed species, z, to perturbations in emissions of species, i, in the case of the OCN scenario (using pseudo observations of ozone, CO, and NO_2) it is defined by

ACPD
15, 4909–4971, 2015

$$\mathbf{K} = \begin{bmatrix} \partial q_{O_3}(\boldsymbol{x},t_1)/\partial x_{NO} & \partial q_{O_3}(\boldsymbol{x},t_1)/\partial x_{CO} & \partial q_{O_3}(\boldsymbol{x},t_1)/\partial x_{VOC} \\ \partial q_{O_3}(\boldsymbol{x},t_2)/\partial x_{NO} & \partial q_{O_3}(\boldsymbol{x},t_2)/\partial x_{CO} & \partial q_{O_3}(\boldsymbol{x},t_2)/\partial x_{VOC} \\ \vdots & \vdots & \vdots \\ \partial q_{O_3}(\boldsymbol{x},t_{N_t})/\partial x_{NO} & \partial q_{O_3}(\boldsymbol{x},t_{N_t})/\partial x_{CO} & \partial q_{O_3}(\boldsymbol{x},t_{N_t})/\partial x_{VOC} \\ \partial q_{CO}(\boldsymbol{x},t_1)/\partial x_{NO} & \partial q_{CO}(\boldsymbol{x},t_1)/\partial x_{CO} & \partial q_{CO}(\boldsymbol{x},t_1)/\partial x_{VOC} \\ \partial q_{CO}(\boldsymbol{x},t_2)/\partial x_{NO} & \partial q_{CO}(\boldsymbol{x},t_2)/\partial x_{CO} & \partial q_{CO}(\boldsymbol{x},t_2)/\partial x_{VOC} \\ \vdots & \vdots & \vdots \\ \partial q_{CO}(\boldsymbol{x},t_{N_t})/\partial x_{NO} & \partial q_{CO}(\boldsymbol{x},t_{N_t})/\partial x_{CO} & \partial q_{CO}(\boldsymbol{x},t_{N_t})/\partial x_{VOC} \\ \partial q_{NO_2}(\boldsymbol{x},t_1)/\partial x_{NO} & \partial q_{NO_2}(\boldsymbol{x},t_1)/\partial x_{CO} & \partial q_{NO_2}(\boldsymbol{x},t_1)/\partial x_{VOC} \\ \partial q_{NO_2}(\boldsymbol{x},t_2)/\partial x_{NO} & \partial q_{NO_2}(\boldsymbol{x},t_2)/\partial x_{CO} & \partial q_{NO_2}(\boldsymbol{x},t_2)/\partial x_{VOC} \\ \vdots & \vdots & \vdots \\ \partial q_{NO_2}(\boldsymbol{x},t_{N_t})/\partial x_{NO} & \partial q_{NO_2}(\boldsymbol{x},t_{N_t})/\partial x_{CO} & \partial q_{NO_2}(\boldsymbol{x},t_{N_t})/\partial x_{VOC} \end{bmatrix} = \frac{\partial \boldsymbol{F}(\boldsymbol{x},t)}{\partial \boldsymbol{x}} \tag{15}$$

where $\mathbf{K}$ has dimensions $N_i \times N$. N_i is the number of species in the emission factor state vector, $\boldsymbol{x}$ and is thus always three. We define N as the total number of observations for all species

$$N = N_t \times N_y \tag{16}$$

where N_t is the number of points in time the model perturbations are sampled and N_y is the number of species whose perturbations are used in the Jacobian. In the case of Eq. (15) $z = O_3$, CO and NO_2 therefore $N_y = 3$. z includes HCHO in the HCN scenario.

ACPD
15, 4909–4971, 2015

Figure 4 plots columns of the Jacobian and it shows that ozone is more sensitive to changes in emissions during the afternoon, and that CO and NO_2 respond to changes in emissions during the rush hour periods.

The key assumption in using the Jacobian is that changes in the emissions can be described approximately by (Rodgers, 2000)

$$F(x) - F(x + \delta x) \approx \mathbf{K}\delta x \tag{17}$$

this assumption has been validated using finite differencing to compare to solutions derived from the right side of Eq. (17).

2.4.3 Emission error characterization

We calculate various statistics to determine the emission estimation performance. First, we determine the a posteriori emission parameter error covariance, which is defined by (Rodgers, 2000)

$$\mathbf{E}\left[\tilde{x}\tilde{x}^{\mathrm{T}}\right] = (\mathbf{S}_{\mathrm{a}}^{-1} + \mathbf{K}^{\mathrm{T}}\mathbf{S}_{n}^{-1}\mathbf{K})^{-1} \tag{18}$$

Next, we calculate the averaging kernel defined by

$$\mathbf{A} = (\mathbf{S}_{\mathrm{a}}^{-1} + \mathbf{K}^{\mathrm{T}}\mathbf{S}_{n}^{-1}\mathbf{K})^{-1}\,\mathbf{K}^{\mathrm{T}}\mathbf{S}_{n}^{-1}\mathbf{K} \tag{19}$$

and the degrees of freedom of signal that is calculated via

$$\text{d.o.f.} = \mathrm{Tr}(\mathbf{A}) \tag{20}$$

where both of these diagnostics provide information on the resolution of the emission retrieval, i.e., the ability of the estimate to uniquely distinguish between the emissions of individual species. While the diagonals of **A** represent the sensitivity of $\hat{x}_i$ to x_i the d.o.f. represents the number of separate emission parameters that can be uniquely retrieved.

ACPD
15, 4909–4971, 2015

2.4.4 Ozone prediction error characterization

Using the a posteriori emission error we can determine the a posteriori ozone prediction error during the prediction period. In order to do this we need to define a new Jacobian matrix, $\mathbf{K}'$, that defines the forward photochemical response during the prediction and monitoring period (day 3) to perturbations in the emissions. Thus, $\mathbf{K}$ and $\mathbf{K}'$ simply differ because $\mathbf{K}$ describes the model response during the observation period as opposed to the prediction and monitoring period. Each element of $\mathbf{K}'$ is $\partial q_z(\boldsymbol{x}, t_j)/\partial \boldsymbol{x}_i$ where j is the index of time denoting when the model is sampled on the 3rd day. The a posteriori ozone prediction error covariance for the 3rd day can be determined by

$$\mathbf{E}\left[\widetilde{q}\widetilde{q}^{\mathrm{T}}\right] = \mathbf{K}'\,\mathbf{E}\left[\widetilde{x}\widetilde{x}^{\mathrm{T}}\right]\mathbf{K}'^{\mathrm{T}} \tag{21}$$

3 Results

3.1 Uncertainty analyses

3.1.1 Assessing observations of CO, NO_2, ozone, and HCHO and the influence of observation error

Emission error characterization and ozone prediction error

In this section we examine the choice of which species to observe in order to best constrain the emissions and improve the ozone prediction, and we look at the three scenarios CN, OCN, and HCN in order to do this. We examine each of these three scenarios across the full range of NO emission scenarios (x_{NO} = 0.5–2.5 with increments of 0.25), and eight different levels of observing error: 1, 5, 10, 25, 50, 100, 250, 500 % (β = 0.1–5). The observing errors are absolute errors represented here as a percentage of the average species concentration over all of the photochemical scenarios. In each of these tests we use pseudo observations obtained by sampling the model true

ACPD
15, 4909–4971, 2015

state at three hour intervals. The observing noises are identical for each compound within a particular scenario. These results include the a posteriori ozone prediction error (calculated by Eq. 21) and the a posteriori emission parameter error (calculated by Eq. 18). Later, we will characterize the emission estimate using the averaging kernel and degrees of freedom of signal diagnostics (see Sect. 3.1.1). We limit our analysis of the observed species to just ozone, CO, NO_2, and HCHO because these gases are be monitored by both ground stations and satellites.

Figure 5 presents the a posteriori ozone prediction errors across the complete range of parameter space and, in each panel, the results from the three observing scenarios. All of the scenarios exhibit similar general behavior in the derived a posteriori ozone prediction errors: a first maximum in ozone prediction uncertainty in the NO_x limited scenarios (x_{NO} = 0.5–0.75), with a consistent minimum in ozone prediction error in the transition region that is both NO_x and VOC limited (x_{NO} = 1.0–1.75), and a second larger maximum in ozone prediction uncertainty in the VOC limited regime (x_{NO} = 2–2.5). Scenario CN (observing only CO and NO_2) yields the highest a posteriori ozone prediction uncertainties of the three scenarios across the range of NO emission scenarios. The inclusion of ozone and HCHO observations in the OCN and HCN scenarios, respectively, reduces the a posteriori ozone prediction uncertainties compared to those from the CN scenario. Scenarios OCN and HCN both show significant improvement in the VOC limited emission scenarios (x_{NO} = 2.0–2.5) with each outperforming the CN scenario by up to 2.4 ppbv. Scenarios OCN and HCN diverge from one another when (x_{NO} = 2.0), which represents the lowest x_{NO} factor that is still VOC limited. In this case, scenario OCN outperforms scenario HCN by up to 1.4 ppbv. Under NO_x limited conditions (x_{NO} = 0.5–1.0), the OCN scenario a posteriori ozone prediction errors show a strong improvement relative to the CN scenario (2.6 ppbv), and a slightly more modest improvement relative to the HCN scenario (1.9 ppbv).

We will now focus on explaining these differences in a posteriori ozone prediction error highlighted above. To gain further insight into this behavior Figs. 6 and 7 show the a posteriori error for x_{NO} and x_{VOC}. Note that the a posteriori error for x_{CO} (not

ACPD
15, 4909–4971, 2015

shown) is invariant with respect to the photochemical regime and is therefore unable to explain any of the observed variability of ozone prediction error over varying x_{NO}.

Figure 6 shows that scenario HCN is able to reduce x_{VOC} a posteriori errors over the largest range of NO emission scenarios, followed by scenario OCN, and scenario CN. This reduction in VOC emission uncertainty in scenario HCN explains why it shows reduced a posteriori ozone prediction error (by up to 2.4 ppbv) compared to the CN scenario under VOC limited conditions. Despite HCHO observations overall providing a better constraint on VOC emission uncertainties under all conditions this improved constraint only leads to lower a posteriori ozone prediction error compared to the OCN scenario in the transition region regimes (x_{NO} = 1.0–1.75) (see Fig. 8 central plot), and under the most VOC limited conditions (x_{NO} >2.0). The exception to this behavior occurs at x_{NO} = 2.0; despite the HCN scenario showing lower x_{VOC} a posteriori errors compared to the OCN scenario the HCN scenario shows higher a posteriori ozone prediction error. This occurs because the a posteriori ozone prediction error is also sensitive to the a posteriori NO emission uncertainties under VOC limited conditions, and ozone is better than HCHO at constraining the NO emission uncertainties.

Figure 7 illustrates that the OCN scenario exhibits the smallest a posteriori NO emission parameter errors compared to any of the other observing scenarios. This is particularly pronounced under VOC limited and NO_x limited conditions. Therefore, ozone is better able to constrain NO emission uncertainties as compared with HCHO under all photochemical conditions, which is because ozone is always more sensitive to changes in NO emissions than HCHO. Note, in the case of VOC limited conditions, ozone is negatively sensitive to NO emissions. As a direct result of this, the OCN scenario ozone a posteriori prediction errors are 2.5 and 1.9 ppbv lower than the CN and HCN scenarios, respectively, while under NO_x limited conditions. Under VOC limited conditions, the OCN scenario shows a posteriori ozone prediction errors that are 2.4 ppbv lower than for the CN scenario. The improved estimation of the NO emissions in the OCN scenario compared to the HCHO scenario only lead to reduced a posteriori ozone prediction errors (by 1.4 ppbv) for the x_{NO} = 2.0 emission case (see Fig. 8). This one exception is

ACPD
15, 4909–4971, 2015

because VOC emissions errors dominate the ozone prediction uncertainty for the other VOC limited cases.

We now briefly explore the benefits of combining all four of the observed species (CO, NO_2, ozone, and HCHO) to make the HOCN scenario. This scenario can improve ozone prediction errors by up to 2.9 and 3.1 ppbv under NO_x and VOC limited conditions, respectively, compared to the CN scenario. Combining ozone and HCHO observations slightly improves ozone prediction errors by up to 0.3 and 0.8 ppbv under NO_x and VOC limited conditions, respectively, compared to the OCN scenario. The differences between the ozone and HCHO combined scenario and the OCN scenario under VOC limited conditions further highlight the potential for HCHO observations to improve ozone prediction errors under the most VOC limited conditions.

Until now, we have not directly discussed the impact of CO observations or of the resolution of CO emission uncertainties within the assimilation framework. We do not show a figure here, but a posteriori CO emission uncertainties are virtually invariant with respect to photochemical regime and to the observing scenario (CN, OCN, or HCN). The a posteriori CO emission uncertainties increase from 1×10^{-5} to 1.1 with increasing observing noise from $\beta = 0.1$ to $\beta = 5$.

Sensitivity test for degraded HCHO observations

The standard HCN scenario described above assumes that the relative observing errors for HCHO are the same as for the other gases. However, within the context of satellite observations, the quality of HCHO observations are likely to be degraded relative to ozone, for instance. This is likely due to the relative magnitude of the absorption cross-sections and interferences from other absorbing gases. We therefore perform a sensitivity test whereby we apply an upward scaling factor to the β of HCHO to increase it by 50 % relative to the other observed gases in the standard HCN scenario. Figure 8 shows that scenario HCN only has lower a posteriori ozone prediction uncertainties over the full range of NO emission scenarios under the optimistic scenario of lower HCHO observation uncertainties (β of HCHO is set to be 50 % lower than that

ACPD
15, 4909–4971, 2015

of ozone), and that in the other scenarios, that we assume would be closer to reality, scenario HCN only out performs scenario OCN in the transition region and for the most VOC sensitive regimes. Under the assumptions of lower ozone observing uncertainty OCN out performs scenario HCN in the NO_x and VOC limited regimes by up to 1.9 ppbv.

Averaging kernel and degrees of freedom of signal

The averaging kernel (Eq. 19) represents the sensitivity of the retrieved emission parameters along the diagonal, i.e., for a particular species, i, to changes in the real emission parameter for species, i. Figure 9 shows the respective diagonals of the averaging kernel (for x_{VOC} and x_{NO}) varying in a manner consistent with the a posteriori parameter errors as shown in Figs. 6 and 7. A comparison of the lower panels indicates that the NO emission parameter estimate using the OCN observing scenario is more sensitive to the true state of the NO emission parameter under both NO_x limited and VOC limited conditions than any of the other observing scenarios. The top panels show that the VOC parameter estimate shows the highest sensitivity to the true state of the VOC emission parameter using the HCN observing scenario.

Consistent with the averaging kernel the degrees of freedom of signal (see Eq. 20), results not shown) indicates that the HCN scenario is better able to uniquely retrieve and resolve the 3 separate emission parameters compared to the OCN scenario. This is because HCHO provides a better constraint on VOC emissions over a wider range of x_{NO} and β. However, ozone in general constrains ozone precursor emissions across a wider variety of emission parameters, specifically for x_{NO}, which allows ozone observations to yield better a posteriori ozone prediction errors. The OCN scenario shows a decrease in the degrees of the freedom of signal under NO_x limited conditions due to the lack of sensitivity of the retrieval to the VOC emission parameter when using these observations.

ACPD
15, 4909–4971, 2015

3.1.2 Observing time and observing frequency

We now examine the sensitivity of the ozone prediction error to the removal of observations at different times during the day. We again use pseudo observations made at 3 hourly intervals, we only use the OCN scenario, we perform these tests of the full range of NO emission scenarios (x_{NO} = 0.5–2.5 with increments of 0.25), and use an observation noise of β = 0.25. Since the first observations are made at 00:00 LT, this means practially that we run our tests by removing observations at 00:00, 03:00, 06:00 (all LT) and so on until each observation within the entire observing window (the first two days of simulation) has been tested.

Figure 10 shows a posteriori ozone prediction errors are most sensitive to the removal of observations during the day particularly during the high emission periods in the morning and afternoon rush hours and particularly so during the period of elevated ozone in the afternoon. The timing and magnitude of the sensitivity and its peak to observation removal varies according to the 9 NO emission scenarios as well. In the more NO_x limited scenarios, x_{NO} = 0.5–1.0, the sensitivity to observation removal is distributed relatively evenly over the entire day. In the VOC limited regimes, x_{NO} = 1.75–2.5, the sensitivity to observation removal is more tightly distributed within the afternoon period and peaks between 3 and 6 p.m. even showing a broad maximum out to 8 p.m. under the most VOC limited conditions. The temporal variability of the maximum sensitivity to observation removal with changing photochemical regime is due to the timing of afternoon peak ozone concentrations. This is because across all of the photochemical regimes maxima in ozone sensitivity to perturbations in emissions coincide with the daytime peak ozone concentration (see Fig. 4). Observations made during these key periods are therefore better able to constrain the emissions uncertainties. Ozone concentrations peak later in the afternoon under more VOC limited conditions compared to the NO_x limited conditions thus explaining some of the variability in maximum sensitivity to observation removal with changing photochemical regime.

ACPD
15, 4909–4971, 2015

Next, we address how observing frequency will affect the ozone prediction error. We run a series of sensitivity tests using a variety of observing frequencies ranging from once a day to once every hour. We carry out these tests across the full range of NO emission scenarios (x_{NO} = 0.5–2.5 with increments of 0.25), and with β = 0.25. Figure 11 shows how a posteriori ozone prediction errors vary with changing observing frequency. Increasing observing frequency causes the largest decreases in a posteriori ozone prediction uncertainty in the VOC limited regime and to a lesser extent in the NO_x limited regime due to the sensitivity of ozone prediction error to unresolved emission parameter errors in those regimes.

3.2 Supporting sensitivity analyses

3.2.1 4-D-variational data assimilation

We now demonstrate the usage and performance of the 4-D-variational data assimilation. Our 4-D-var framework solves the non-linear estimation problem whereby it optimizes the ozone precursor emissions and then estimates a posteriori ozone mixing ratios (the forecast). We run the system across the full range of photochemical conditions (x_{NO} = 0.5–2.5) and for the CN, OCN and HCN scenarios whilst assuming low levels of observational error (β = 0.1) represented in the observation error covariance matrix.

The results shown in Table 4 indicate that scenarios OCN and HCN yield acceptable prediction error under these idealised conditions (β = 0.1) within this prototype framework for all photochemical conditions. The more limited success of scenario CN (observations of CO and NO_2) is due to the lower sensitivity of CO and NO_2 observations to the emissions of VOCs across all NO_x emission scenarios, and of the low sensitivity of CO observations to the emissions of NO. The magnitude of the adjoint sensitivities guides the L-BFGS algorithm (Zhu et al., 1997) to the global minimum. In cases where the adjoint sensitivities are low, e.g., in VOC limited conditions using the

ACPD
15, 4909–4971, 2015

CN scenario, the optimization routine may only be able to find a non-global minimum, which leads to larger a posteriori emission factor errors, $\hat{\boldsymbol{x}} - \boldsymbol{x}t$.

Table 4 indicates that there is variability of a posteriori peak ozone prediction error over changing photochemical regime and x_{NO} for each observing scenario CN, OCN, and HCN. This variability with x_{NO} is due in part to the variations in modeled ozone sensitivity to the different ozone precursor emission parameters, $\partial q_{O_3}(\boldsymbol{x},t)/\partial x_i$, and the a posteriori emission parameter errors (i.e., $\hat{\boldsymbol{x}} - \boldsymbol{x}t$). Generally, large sensitivity of predicted ozone to the emissions of ozone precursors, $\partial q_{O_3}(\boldsymbol{x},t)/\partial x_i$, combined with unresolved ozone precursor emission parameter errors can lead to larger a posteriori peak ozone prediction error. For instance, in the NO_x limited regimes (x_{NO} = 0.5–1.0) large residual error in the element of $\hat{\boldsymbol{x}}$ corresponding to NO emissions would lead to large a posteriori ozone errors.

One example of this phenomenon occurs in the case of photochemically VOC limited scenarios (i.e., x_{NO} = 1.75–2.5). Table 5 shows the variability of a posteriori VOC emission errors with x_{NO} and observing scenario. For observing scenario CN there is large unresolved error in x_{VOC} (Table 5) as in this case the size of the adjoint sensitivities is insufficient to guide the L-BFGS algorithm to the global minimum and the solutions represent local minima. This leads to larger a posteriori ozone prediction error as compared to scenarios OCN and HCN (see Table 4), which are better able to resolve errors in VOC emissions.

Thus, there are a rather complex set of factors interacting to cause these resulting a posteriori prediction errors and the analysis of the results is limited to identifying relationships between the observing scenario, the photochemical regime, the adjoint sensitivities and the resulting ozone a posteriori prediction error. This demonstrates the utility of the analytical model in allowing a far more in-depth analysis. Overall, the 4-D-variational data assimilation framework seems capable of resolving emission uncertainties and in turn reducing ozone prediction error. This successful demonstration of the framework is a necessary but not sufficient condition for systems based upon more complex photochemical models to have ozone predictive skill.

ACPD
15, 4909–4971, 2015

3.2.2 Examining day-to-day varibility and probing emission solution sensitivity to diurnal emission variability

We investigate the sensitivity of the forward photochemical model ozone mixing ratios, obtained via the 4-D-var ozone prediction and the 4-D-var emissions estimate, to a range of assumed emission diurnal profiles. We use the following profiles selected arbitrarily to test the model sensitivity: constant, sine wave, square wave, and offsets of the existing profile by 1 and 2 h shifts both forward and backward in time (see Fig. 1). These alternate emission profiles are taken to represent the new true state, $\boldsymbol{x}t$, (using $x_{\mathrm{NO}} = 0.75$) and are used to generate the pseudo observations (using $\beta = 0.1$). We then attempt the assimilation using the pseudo observations generated from the alternative emission scenarios whilst assuming that the emissions temporal variability is the standard variability. The alternate emission profiles test the robustness of the 4-D-variational data assimilation method to diurnal uncertainty in the emissions.

Table 6 indicates that the forward model shows peak ozone mixing ratios diverging from the base case run (standard assumed emission variability with $x_{\mathrm{NO}} = 0.75$) by up to 10.6 ppbv and that the forward model ozone mixing ratios are sensitive to the assumption of the diurnal emission variability. In addition, Table 6 shows that the 4-D-variational data assimilation is able to achieve a posteriori peak ozone prediction errors of up to 2.4 ppbv relative to the true state, as defined by the perturbed scenario, despite using the unperturbed diurnal emission scenario as its emission variability. Despite the relative success of the a posteriori peak ozone prediction (only a maximum ozone prediction error of 2.4 ppbv) under these more challenging conditions the assimilation performs poorly in terms of the a posteriori emission factor error. Errors range up to 0.46 (18–92 %), 0.17 (17 %), and 7.0 (108 %) for x_{NO}, x_{CO}, and x_{VOC} (relative to true scaling factors of 0.5–5.0, 1.0, and 6.5, respectively) and thus emission inversion success is strongly affected by errors in the assumed diurnal variability of ozone precursor emissions. In summary, we demonstrate forward model ozone sensitivity to perturbations in the diurnal variability of ozone precursor emissions, relative insensitivity of the

ACPD
15, 4909–4971, 2015

4-D-variational data assimilation a posteriori prediction error to mismatches in the assumed vs. observed diurnal variability of ozone precursor emissions, and sensitivity of the emissions inversion success to mismatches in the assumed vs. true emissions variability.

We also explore what the real-world variability is in terms of day-to-day emission magnitude and apparent emission profile for a specific case. This investigation is necessary because we assume that there is no day-to-day variation in either emission magnitude or the profile of the emissions. Observation data for ozone, CO and NO_2 collected by the South Coast Air Quality Monitoring District at Wilson Ave., Pasadena (see Fig. 12) show that this assumption is valid for a consecutive three day period consisting of Wednesday, Thursday, and Friday. Our assumption of no day-to-day variability in ozone precursor emissions is reasonable for this region across a three day period such as this. These findings are fully consistent with previous work studying air quality in Southern California (Blanchard and Fairley, 2001; Blanchard and Tanenbaum, 2003).

3.2.3 Emission inversion and ozone predictive skill sensitivity to VOC species selection

We conducted a sensitivity test whereby we represent VOC emission uncertainties with uncertainties in the emission of ethane, which is a less reactive VOC compared to ethene. We found that that the VOC emission inversion is severely degraded by building the Jacobian by perturbing x_{ethane} as opposed to x_{ethene} across the three scenarios. The a posteriori x_{VOC} parameter error relaxes to our chosen a priori of 1.5 to within 1 significant figure for most of the scenarios explored. However, this does not affect ozone prediction error since the degraded VOC emission uncertainty is mitigated by the lower reactivity of ethane compared to ethene. As a result, the sensitivity of ozone to that uncertainty is therefore lower.

ACPD
15, 4909–4971, 2015

4 Discussion and conclusions

We addressed a set of key questions to determine how characteristics of observations of ozone and its precursors affect one's ability to constrain ozone precursor emissions and consequently to predict ozone when using an idealised prognostic air quality model coupled to a data assimilation framework. These questions consisted of which species to observe, how well to observe them, how often to make observations, when to make them during the diurnal cycle, and how soon to observe before making a prediction. Further to this, we were interested in how the answers to these questions changed according to varying photochemical regime (from NO_x to VOC limited conditions for ozone formation). These questions are relevant to determining, in a very coarse way, how the various observing platforms (i.e., LEO and GEO satellites) and ground monitoring networks are able to support air quality research and forecasting.

We used a framework consisting of a photochemical box model using idealised meteorology, its adjoint, and a 4-D-variational data assimilation system setup to constrain ozone pre-cursor emission uncertainties (NO_x, CO, and VOCs). The photochemical box model used idealised meteorology that represented stagnant summer weather conditions. Using linear analysis to assess the framework's prediction uncertainties we carried out a series of sensitivity analyses to test the performance of the forecasting framework under a range of different observing scenarios. This consisted of using various sets of pseudo observations. We examined the effect of changing which four species were observed (CO, NO_2 and HCHO, CO, and NO_2), of varying the observation noise, of changing the observing frequency, and of changing the time during the day when observations are made.

We were able to demonstrate that the 4-D-var framework was able to constrain ozone precursor emissions and consequently that it was able to reduce ozone prediction uncertainties and provide an adequate ozone forecast under the idealised conditions that we used. This therefore demonstrated our framework's relevance to future air quality forecasting systems that might utilize state of the art assimilation and observations

ACPD
15, 4909–4971, 2015

made using either the ground station network or from orbiting satellites. Then, using the linear analysis to estimate the prediction uncertainties, we were able to derive a series of general conclusions that are discussed below.

4.1 The effect of changing the observed species

Our results show that the variability of ozone prediction error with both photochemical regime and observing species scenario (CN, OCN and HCN) is complex and no single observed species is ideal for all photochemical conditions.

Under NO_x limited conditions ozone prediction error is strongly controlled by the a posteriori NO emission errors and therefore observations of NO_2 and ozone would be highly advantageous. Ozone provides a particularly good constraint upon NO emissions under very NO_x limited and VOC limited conditions. The value of NO_2 observations in constraining NO emissions improves as the NO_x lifetime increases under the somewhat less NO_x limited conditions (x_{NO} = 1.0–1.25). Much of the troposphere is in fact highly NO_x limited outside of the most polluted areas (Duncan et al., 2010).

Under VOC limited conditions ozone prediction error is sensitive to both a posteriori x_{NO} (due to the negative sensitivity of ozone to NO_x) and x_{VOC} errors and thus observations of ozone, HCHO and NO_2 allow significant improvements in ozone prediction error. Assimilating ozone, therefore, allows constraints to be placed upon VOC and NO emission uncertainties. HCHO provides an excellent constraint upon reactive VOC emissions, which due to their reactivity are more relevant to air quality compared to less reactive VOCs. NO_2 provides an excellent constraint upon NO emissions under VOC limited conditions; more than under NO_x limited conditions due to the longer NO_x lifetime. Despite the fact that large geographical portions of the US are NO_x limited a disproportionately large percentage of the populous live within or are exposed to ozone arising from VOC limited conditions due to the significant extent of urbanization within the US. Large urbanized areas of the South West that lack significant native vegetative biomass typically have a larger VOC limited regime that extends over the urban as well as sub-urban areas. In contrast, US cities in the East are located in regions

ACPD
15, 4909–4971, 2015

with often dense vegetative biomass, e.g., Atlanta, and thus the VOC limited region is far more geographically limited to the urban center itself. Therefore, improving ozone predictive skill within VOC limited conditions will not yield forecasting improvements over a wide geographical area but will yield improvements within certain regions with large populations.

Our findings with respect to the utility of NO_2 and HCHO observations for constraining NO_x and VOC emissions, respectively, and in turn for improving ozone estimation are broadly consistent with the findings of Zhang et al. (2008), which used satellite observations of NO_2 and HCHO in conjunction with 4-D-variational data assimilation to solve for NO_2 and HCHO emissions and to improve the model's ozone estimation. One should note, however, that our work goes further by demonstrating how the efficacy of NO_2 and HCHO observations varies according to photochemical regime. Similar to (Elbern et al., 2000, 2007), we demonstrate the use of ozone in this regard. Our work offers an extension to Elbern et al. (2000, 2007) by considering the photochemical regime and by considering other observations simultaneously.

Note that the statements above regarding the need to constrain NO and VOC emissions under NO_x and VOC limited conditions, respectively, are what we should expect. Further, the use of ozone to constrain either NO_x or VOC emissions in either of the respective photochemical regimes is fully consistent with existing theory relating to ozone control strategies (Sillman, 1993) and our understanding of factors controlling ozone at regional and continental scales (Jacob et al., 1993). This was one motivation for us to explore this problem.

There is one further advantage to observations of ozone and HCHO made under VOC limited conditions. Often, plumes of NO_x polluted and VOC limited air can be exported from regions that are VOC limited into areas that are NO_x limited, and this can lead to significant temporal variability in the photochemical regime in the regions surrounding an urban center. Therefore, observations of HCHO and ozone in addition to NO_2 observations could help to understand such events and in turn reduce ozone prediction errors.

ACPD
15, 4909–4971, 2015

We have not performed a sensitivity test to directly the effect CO observations have upon ozone a posteriori prediction errors. However, we can briefly address their potential impact within the OCN scenario by examining the jacobian matrix (see Fig. 4) that shows that ozone is relatively insensitive to perturbations in CO emissions and, therefore, also to a posteriori CO emission uncertainties.

4.2 Observation error

We now make some broad conclusions regarding the observation uncertainties. Both the OCN and standard HCN scenarios achieve a posteriori ozone prediction errors of 2.4–6.1 and 1.9–6.3 ppbv, respectively, when absolute errors equivalent to 33 % of the average over polluted regions were used. Even though the OCN and HCN scenarios compared favourably to one another in terms of their a posteriori ozone prediction errors, when we considered more realistic observational noise on the HCHO observations, the performance of the HCN scenario was degraded to 2.2–6.9 ppbv (33 % noise level). In comparison, for the same noise level, the CN scenario achieved ozone prediction errors of 2.5–8.4 ppbv. Only when the noise level was reduced to 25 % were the OCN and HCN scenarios able to achieve ozone prediction errors of 5 ppbv or less. At 10 % noise ozone prediction errors of less than 2.5 ppbv were consistently attained for both OCN and HCN. This strongly points towards there being a good payoff in forecast accuracy with reducing observation error. Further work in a 3-D framework would be required in order to determine how these ozone forecast errors translate into the context of real air quality forecasting. For instance, it might be possible to calculate the probability of detection or false alarm rate statistics similar to the work carried out by Hache et al. (2014).

Connecting this to real instrument profiles and real observations, and how these might perform in a real assimilation system, is beyond the scope of this study. The furthest we can take this point is to note that the resulting prediction uncertainties for a particular observation noise scenario are optimistic and represent the lowest error that could be expected. This is because of reduced complexity in our model's represen-

ACPD
15, 4909–4971, 2015

tation of its spatial domain and its meteorology and because of the way we represented the errors on our observations, which in reality would be more complex.

4.3 Temporal considerations

Concerning the temporal sampling of observations, there is strong sensitivity of ozone prediction error to observation removal in the daytime, particularly in the afternoon, and therefore observations made during the day present greater returns in terms of improved forecasting ability. The NO_x limited regimes favour observations made throughout the day with increased observing density close to 3 p.m. The VOC limited regimes favour a greater concentration of observations within the afternoon even up to 6 p.m. in the most VOC limited cases. These differing results for the two different photochemical regimes are consistent with existing knowledge of photochemistry and NO_x lifetime. The main underlying factors controlling this are the changing time at which ozone peaks and the time of day that emissions occur that contribute to that peak. Under VOC limited conditions ozone peaks later in the day due to the reduced ozone lifetime and the slower recovery of HO_x radicals (suppressed by NO_x) that occurs after the night time period. The NO_x limited scenarios also show a smaller peak in the morning. This smaller peak is present due to the observations of ozone and NO_2 during the morning rush hour that better allow NO_x emissions to be constrained. The presence of the smaller peak also indicates that peak afternoon ozone concentrations are sensitive to the morning rush hour emissions of NO_x; this is possible due to the longer ozone lifetime present under NO_x limited conditions.

We demonstrate that the ozone prediction error is sensitive to the frequency of observation. We show that ozone prediction errors vary between negligible to up to 12.5 ppbv as the observing frequency varies between once per hour to once per day, respectively. The ozone prediction error is maximised within either the NO_x limited or VOC limited regimes. We find very similar levels of ozone prediction error for the scenarios that observe once every hour and every three hours (1.8–3.2 ppbv compared to 2.2–4.8 ppbv, respectively), and that ozone prediction errors greater than 5 ppbv only emerge for ob-

ACPD
15, 4909–4971, 2015

serving scenarios using a frequency of six hours or more. The fact that our forecasting system performs best using observations made at a frequency of three hours or less highlights the temporal sampling advantage posed by the ground observation network relative to observing systems with lower observing frequency, i.e., a satellite in LEO configuration.

4.4 Implications for emission inversion

Aside from the relevance of these results to air quality forecasting and research in general, we believe these results are also relevant for emission and flux estimation via inversion methologies. Our prototype framework is mechanically very similar to other work using 4-D-variational data assimilation methologies (Elbern et al., 2000, 2007; Henze et al., 2009; Stavrakou et al., 2009; Kopacz et al., 2010) using chemistry transport models that have focused on emission inversion. Much of the emission inversion performance shown in this study is driven by the photochemistry, and it is reasonable to suppose that some of our results are relevant to future work conducted using 4-D-variational data assimilation in emission inversion studies. From this premise, we recommend that emission inversion studies for NO_x utilize both observations of NO_2 and ozone since ozone observations add information to the x_{NO} estimation under both strongly positively and negatively NO_x limited conditions and NO_2 observations constrain emission parameter uncertainties the most under the more VOC limited conditions. Thus, these two observations are complementary to each other. Likewise, for emission inversions of VOCs we recommend observations of HCHO and ozone since HCHO observations can constrain VOC emission uncertainties under a wide variety of photochemical conditions and ozone can constrain VOC emission uncertainties under VOC limited conditions.

Previous studies have shown that NO_2 (Konovalov et al., 2006; Zhang et al., 2008; Muller and Stavrakou, 2005) and HCHO (Stavrakou et al., 2009; Millet et al., 2006, 2008; Palmer et al., 2003, 2006; Zhang et al., 2008) observations can constrain NO_x and VOC emissions, respectively. Although one could have inferred that combining

ACPD
15, 4909–4971, 2015

ozone observations with either NO_2 or HCHO observations would be beneficial to our knowledge we are the first to demonstrate this novel approach, and we have shown that it could be highly advantageous.

It should be noted that the conclusions regarding VOC emission inversion are sensitive to our choice of representing VOC emission uncertainties with ethene. The success of the VOC emission inversion is significantly limited by solving for ethane emission uncertainties. This is due to the lack of impact on secondary chemical species such as HCHO. This is one reason why previous emission inversion modeling studies have focused on constraining reactive VOCs like isoprene (Millet et al., 2006, 2008; Palmer et al., 2003, 2006).

Concerning CO, all of the observing scenarios (CN, OCN, and HCN) performed equally well at constraining CO emission uncertainties since all these scenarios included observations of CO. Indeed, the jacobian for CO with respect to CO emission perturbations shown in Fig. 4 clearly shows a strong sensitivity of CO to changes in its own emissions. On the other hand, Fig. 4 shows much lower sensitivity of CO to the emissions of NO or VOCs. These results are fully consistent with expectations due to the relatively low reactivity of CO and its potential to produce ozone on short timescales and of the lack of a strong chemical connection between NO_x levels and resulting CO concentrations. In the latter case, there is a link due to the way that NO_x can perturb OH, but due to the relative unreactivity of CO this leads to only weak sensitivity in the jacobian. Consistent with this, there have already been several studies that use observations of CO to constrain CO emissions (Muller and Stavrakou, 2005; Kopacz et al., 2010; Arellano et al., 2006).

In the supporting sensitivity analysis probing emission solution sensitivity to diurnal emission variability we demonstrate that emission inversions are potentially highly sensitive to the assumed variability of the emissions and that even perfect observations would lead to such errors. In our system such emission inversion errors would be hard to characterize in the absence of any information regarding the true state of the emissions variability. We recommend that such uncertainties should be considered

ACPD
15, 4909–4971, 2015

and characterized in emissions inversion studies. Currently diurnal emission variabilities are determined in the process of building bottom-up emission inventories. Although our prototype assimilation system can only currently solve for time independent scaling factors it could be modified to solve for time dependent scaling factors and the diurnal emissions variability. Future assimilation forecasting systems should also possess this ability to solve for time dependent emission scaling factors. Observations that adequately capture the diurnal variability of pollutants will be essential to making this leap from time independent solutions to time dependent solutions.

4.5 Implications for GEO and LEO satellites

In the previous sections we have motivated the potential utility of surface or boundary layer ozone, CO, NO_2, and HCHO observations either in the context of improving ozone forecasting or for emission inversions. Ground station networks that implicitly sample boundary layer air are already in place across the American and European continents. However, non of the current generation of LEO satellites possesses a reliable means of attaining instrument sensitivity to the boundary layer for these gases. If future GEO stationary satellite instruments (GEO-CAPE/TEMPO, GEMS, and Sentinel-4) wish to fully take advantage of their simultaneous potential for superb coverage and temporal sampling and wish to fully contribute to state of the art ozone air quality forecasting, then attaining sensitivity to the boundary layer is essential and should be a high priority aim.

The heightened importance of observations made during the morning and mid to late afternoon raises the question of whether making more targetted observations, for instance made during the morning and evening rush hours, would be able to support ozone forecasting even further. There are various observing systems that would be able to provide this capability, such as several combined LEO missions or ground stations or a GEO mission with increased temporal sampling capability during those periods. Investigating these questions in the future would be of interest to us.

ACPD
15, 4909–4971, 2015

Our forecasting system is better able to improve the ozone prediction using observations made during the day as opposed to the night. In the context of satellites, and remembering that our idealised case ignores the effects of transport, this indicates that instruments capable of observing during the night, such as those observing in the TIR, do not offer a significant advantage over instruments restricted to making measurements during the day time. Of course, if the effects of transported pollution were to be considered, making observations during the night could offer additional utility by improving the estimated contribution to the pollution made by this process. For instance, this could provide advance warning of the trajectory of a pollution plume. This is therefore a limitation of this work that we are not able to explore such effects using a model with only idealised meteorology.

Our forecasting system (and the emission inversion) performs best using observations made at a frequency of three hours or less. This highlights the temporal sampling advantage posed by satellites in a GEO configuration as opposed to those in LEO. Currently, the proposed observing frequencies for the future GEO missions (Lahoz et al., 2012) and the current ground monitoring network are at least at one hour. LEO satellites, on the other hand, can not attain high frequency sampling without a large number of satellites being employed (Lahoz et al., 2012). In isolation, a single LEO satellite with a sampling frequency of between 1 and 16 days is perhaps inadequate for the purpose of constraining precursor emissions at the regional scale or for supporting air quality forecasting. Another consideration is that observing frequencies of three hours or more might not be adequate for studying the diurnal cycle of pollutants and for forecasting systems that use 3-D-var, for instance, to update ozone concentrations. Note that the nature of our framework for performing these tests (i.e., a box model using only idealised meteorology) places limitations on our conclusions such that the performance of the higher frequency observing scenarios (3 h or less) may be too optimistic. Thus, observing at three hours may too be insufficient to constrain ozone precursor emissions.

ACPD
15, 4909–4971, 2015

Acknowledgements. P. D. Hamer thanks ORAU and the NPP program for funding and support, D. Millet and D. Jacob for helpful discussion and comments, and A. M. Aghedo for help and formatting tips. D. K. Henze supported by NASA Applied Science Program. We thank Météo France and CNRM for support and for financing the publication of the article.

References

Arellano, A., Kasibhatla, P., Giglio, L., van der Werf, G., Randerson, J., and Collatz, G.: Time-dependent inversion estimates of global biomass-burning CO emissions using Measurement of Pollution in the Troposphere (MOPITT) measurements, J. Geophys. Res.-Atmos., 111, D09303, doi:10.1029/2005JD006613, 2006. 4913, 4943

Blanchard, C. and Fairley, D.: Spatial mapping of VOC and NO_x-limitation of ozone formation in central California, Atmos. Environ., 35, 3861–3873, doi:10.1016/S1352-2310(01)00153-4, 2001. 4912, 4936

Blanchard, C. and Tanenbaum, S.: Differences between weekday and weekend air pollutant levels in southern California, JAPCA J. Air Waste Ma., 53, 816–828, 2003. 4912, 4936

Bowman, K. W., Jones, D. B. A., Logan, J. A., Worden, H., Boersma, F., Chang, R., Kulawik, S., Osterman, G., Hamer, P., and Worden, J.: The zonal structure of tropical O_3 and CO as observed by the Tropospheric Emission Spectrometer in November 2004 – Part 2: Impact of surface emissions on O_3 and its precursors, Atmos. Chem. Phys., 9, 3563–3582, doi:10.5194/acp-9-3563-2009, 2009. 4913

Chai, T., Carmichael, G. R., Tang, Y., Sandu, A., Hardesty, M., Pilewskie, P., Whitlow, S., Browell, E. V., Avery, M. A., Nedelec, P., Merrill, J. T., Thompson, A. M., and Williams, E.: Four-dimensional data assimilation experiments with International Consortium for Atmospheric Research on Transport and Transformation ozone measurements, J. Geophys. Res.-Atmos., 112, D12S15, doi:10.1029/2006JD007763, 2007. 4913

Dabberdt, W., Carroll, M., Baumgardner, D., Carmichael, G., Cohen, R., Dye, T., Ellis, J., Grell, G., Grimmond, S., Hanna, S., Irwin, J., Lamb, B., Madronich, S., McQueen, J., Meagher, J., Odman, T., Pleim, J., Schmid, H., and Westphal, D.: Meteorological research needs for improved air quality forecasting – report of the 11th prospectus development team of the US Weather Research Program, B. Am. Meteorol. Soc., 85, 563–586, doi:10.1175/BAMS-85-4-563, 2004. 4911

ACPD
15, 4909–4971, 2015

Dabberdt, W. F., Carroll, M. A., Appleby, W., Baumgardner, D., Carmichael, G., Davidson, P., Doran, J. C., Dye, T. S., Grimmond, S., Middleton, P., Neff, W., and Zhang, Y.: USWRP workshop on air quality forecasting, B. Am. Meteorol. Soc., 87, 215–221, 2006. 4911

Daescu, D., Sandu, A., and Carmichael, G.: Direct and adjoint sensitivity analysis of chemical kinetic systems with KPP: II – Numerical validation and applications, Atmos. Environ., 37, 5097–5114, doi:10.1016/j.atmosenv.2003.08.020, 2003. 4918, 4922

Damian, V., Sandu, A., Damian, M., Potra, F., and Carmichael, G.: The kinetic preprocessor KPP – a software environment for solving chemical kinetics, Comput. Chem. Eng., 26, 1567–1579, 2002. 4918

Dufour, G., Eremenko, M., Orphal, J., and Flaud, J.-M.: IASI observations of seasonal and day-to-day variations of tropospheric ozone over three highly populated areas of China: Beijing, Shanghai, and Hong Kong, Atmos. Chem. Phys., 10, 3787–3801, doi:10.5194/acp-10-3787-2010, 2010. 4913

Duncan, B. N., Yoshida, Y., Olson, J. R., Sillman, S., Martin, R. V., Lamsal, L., Hu, Y., Pickering, K. E., Retscher, C., Allen, D. J., and Crawford, J. H.: Application of OMI observations to a space-based indicator of NO_x and VOC controls on surface ozone formation, Atmos. Environ., 44, 2213–2223, doi:10.1016/j.atmosenv.2010.03.010, 2010. 4913, 4938

Elbern, H., Schmidt, H., Talagrand, O., and Ebel, A.: 4D-variational data assimilation with an adjoint air quality model for emission analysis, Environ. Modell. Softw., 15, 539–548, doi:10.1016/S1364-8152(00)00049-9, Meeting on Air Pollution Modeling and Simulation, Paris, France, OCT, 1998, 2000. 4939, 4942

Elbern, H., Strunk, A., Schmidt, H., and Talagrand, O.: Emission rate and chemical state estimation by 4-dimensional variational inversion, Atmos. Chem. Phys., 7, 3749–3769, doi:10.5194/acp-7-3749-2007, 2007. 4917, 4939, 4942

Eller, P., Singh, K., Sandu, A., Bowman, K., Henze, D. K., and Lee, M.: Implementation and evaluation of an array of chemical solvers in the Global Chemical Transport Model GEOS-Chem, Geosci. Model Dev., 2, 89–96, doi:10.5194/gmd-2-89-2009, 2009. 4918, 4922

Finlayson-Pitts, B. and Pitts, J.: Tropospheric air pollution: ozone, airborne toxics, polycyclic aromatic hydrocarbons, and particles, Science, 276, 1045–1052, doi:10.1126/science.276.5315.1045, 1997. 4912

Fishman, J., Creilson, J. K., Parker, P. A., Ainsworth, E. A., Vining, G. G., Szarka, J., Booker, F. L., and Xu, X.: An investigation of widespread ozone damage to the soybean crop

ACPD
15, 4909–4971, 2015

in the upper Midwest determined from ground-based and satellite measurements, Atmos. Environ., 44, 2248–2256, doi:10.1016/j.atmosenv.2010.01.015, 2010. 4913
Fumagalli, I., Gimeno, B., Velissariou, D., De Temmerman, L., and Mills, G.: Evidence of ozone-induced adverse effects on crops in the Mediterranean region, Atmos. Environ., 35, 2583–2587, 2001. 4911
Gardner, M. and Dorling, S.: Statistical surface ozone models: an improved methodology to account for non-linear behaviour, Atmos. Environ., 34, 21–34, 2000. 4911
Grell, G. A., Peckham, S. E., Schmitz, R., McKeen, S. A., Frost, G., Skamarock, W. C., and Eder, B.: Fully coupled "online" chemistry within the WRF model, Atmos. Environ., 39, 6957–6975, doi:10.1016/j.atmosenv.2005.04.027, 2005. 4911
Hache, E., Attié, J.-L., Tourneur, C., Ricaud, P., Coret, L., Lahoz, W. A., El Amraoui, L., Josse, B., Hamer, P., Warner, J., Liu, X., Chance, K., Höpfner, M., Spurr, R., Natraj, V., Kulawik, S., Eldering, A., and Orphal, J.: The added value of a visible channel to a geostationary thermal infrared instrument to monitor ozone for air quality, Atmos. Meas. Tech., 7, 2185–2201, doi:10.5194/amt-7-2185-2014, 2014. 4914, 4940
Hakami, A., Henze, D. K., Seinfeld, J. H., Singh, K., Sandu, A., Kim, S., Byun, D., and Li, Q.: The adjoint of CMAQ, Environ. Sci. Technol., 41, 7807–7817, 2007. 4917
Henze, D. K., Seinfeld, J. H., and Shindell, D. T.: Inverse modeling and mapping US air quality influences of inorganic $PM_{2.5}$ precursor emissions using the adjoint of GEOS-Chem, Atmos. Chem. Phys., 9, 5877–5903, doi:10.5194/acp-9-5877-2009, 2009. 4942
IPCC: Inter-Governmental Panel on Climate Change Fourth Assessment Report Working Group 1 Report, "The Physical Basis", Cambridge University Press, Cambridge, United Kingdom and New York, NY, USA, 2007. 4911
Jacob, D., Logan, J., Gardner, G., Yevich, R., Spivakovsky, C., Wofsy, S., Sillman, S., and Prather, M.: Factors regulating ozone over the United-States and its export to the global atmosphere, J. Geophys. Res.-Atmos., 98, 14817–14826, doi:10.1029/98JD01224, 1993. 4912, 4916, 4939
Jenkin, M., Saunders, S., and Pilling, M.: The tropospheric degradation of volatile organic compounds: a protocol for mechanism development, Atmos. Environ., 31, 81–104, 1997. 4918
Jones, D. B. A., Bowman, K. W., Logan, J. A., Heald, C. L., Liu, J., Luo, M., Worden, J., and Drummond, J.: The zonal structure of tropical O_3 and CO as observed by the Tropospheric Emission Spectrometer in November 2004 – Part 1: Inverse modeling of CO emissions, Atmos. Chem. Phys., 9, 3547–3562, doi:10.5194/acp-9-3547-2009, 2009. 4913

ACPD
15, 4909–4971, 2015

Kang, D., Mathur, R., and Rao, S. T.: Real-time bias-adjusted O-3 and PM2.5 air quality index forecasts and their performance evaluations over the continental United States, Atmos. Environ., 44, 2203–2212, doi:10.1016/j.atmosenv.2010.03.017, 2010. 4911

Konovalov, I. B., Beekmann, M., Richter, A., and Burrows, J. P.: Inverse modelling of the spatial distribution of NO_x emissions on a continental scale using satellite data, Atmos. Chem. Phys., 6, 1747–1770, doi:10.5194/acp-6-1747-2006, 2006. 4913, 4942

Kopacz, M., Jacob, D. J., Fisher, J. A., Logan, J. A., Zhang, L., Megretskaia, I. A., Yantosca, R. M., Singh, K., Henze, D. K., Burrows, J. P., Buchwitz, M., Khlystova, I., McMillan, W. W., Gille, J. C., Edwards, D. P., Eldering, A., Thouret, V., and Nedelec, P.: Global estimates of CO sources with high resolution by adjoint inversion of multiple satellite datasets (MOPITT, AIRS, SCIAMACHY, TES), Atmos. Chem. Phys., 10, 855–876, doi:10.5194/acp-10-855-2010, 2010. 4913, 4942, 4943

Kurokawa, J.-I., Yumimoto, K., Uno, I., and Ohara, T.: Adjoint inverse modeling of NO_x emissions over eastern China using satellite observations of NO2 vertical column densities, Atmos. Environ., 43, 1878–1887, doi:10.1016/j.atmosenv.2008.12.030, 2009. 4913

Lahoz, W. A., Peuch, V. H., Orphal, J., Attié, J.-L., Chance, K., Liu, X., Edwards, D., Elbern, H., Flaud, J. M., Claeyman, M., and El Amraoui, L.: Monitoring air quality from space, the case for the geostationary platform, B. Am. Meteorol. Soc., 93, 221–233, doi:10.1175/BAMS-D-11-00045.1, 2012. 4913, 4945

Landgraf, J. and Hasekamp, O. P.: Retrieval of tropospheric ozone: the synergistic use of thermal infrared emission and ultraviolet reflectivity measurements from space, J. Geophys. Res.-Atmos., 112, D08310, doi:10.1029/2006JD008097, 2007. 4914

Lee, S., Hong, Y., Song, C., Lee, M., Ryoo, S., Kim, J., Yong, S., Bhartia, P. K., Park, R., Woo, J., Kim, Y. J., Song, C. H., Kim, J. H., Lee, K., Ho, C., Park, S. K., Lee, Y., Lee, J., Kim, M., Eom, Y., and Hong, J.: Geostationary Environment Monitoring Spectrometer(GEMS) Onboard MP-GEOSAT (Multi Purpose Geostationary Satellite) over Asia-Pacific Region, AGU Fall Meeting Abstracts, vol. 1, San Francisco, USA, 2009. 4914

Martin, R. V.: Satellite remote sensing of surface air quality, Atmos. Environ., 42, 7823–7843, doi:10.1016/j.atmosenv.2008.07.018, 2008. 4913

Millet, D. B., Jacob, D. J., Turquety, S., Hudman, R. C., Wu, S., Fried, A., Walega, J., Heikes, B. G., Blake, D. R., Singh, H. B., Anderson, B. E., and Clarke, A. D.: Formaldehyde distribution over North America: implications for satellite retrievals of

ACPD
15, 4909–4971, 2015

formaldehyde columns and isoprene emission, J. Geophys. Res.-Atmos., 111, D24S02, doi:10.1029/2005JD006853, 2006. 4942, 4943
Millet, D. B., Jacob, D. J., Boersma, K. F., Fu, T.-M., Kurosu, T. P., Chance, K., Heald, C. L., and Guenther, A.: Spatial distribution of isoprene emissions from North America derived from formaldehyde column measurements by the OMI satellite sensor, J. Geophys. Res.-Atmos., 113, D02307, doi:10.1029/2007JD008950, 2008. 4913, 4942, 4943
Müller, J.-F. and Stavrakou, T.: Inversion of CO and NO_x emissions using the adjoint of the IMAGES model, Atmos. Chem. Phys., 5, 1157–1186, doi:10.5194/acp-5-1157-2005, 2005. 4942, 4943
Murphy, J., Delucchi, M., McCubbin, D., and Kim, H.: The cost of crop damage caused by ozone air pollution from motor vehicles, J. Environ. Manage., 55, 273–289, 1999. 4911
Mustafa, M.: Biochemical basis of ozone toxicity, Free Radical Bio. Med., 9, 245–265, 1990. 4911
Nali, C., Pucciariello, C., and Lorenzini, G.: Ozone distribution in central Italy and its effect on crop productivity, Agr. Ecosyst. Environ., 90, 277–289, 2002. 4911
Otte, T., Pouliot, G., Pleim, J., Young, J., Schere, K., Wong, D., Lee, P., Tsidulko, M., McQueen, J., Davidson, P., Mathur, R., Chuang, H., DiMego, G., and Seaman, N.: Linking the eta model with the Community Multiscale Air Quality (CMAQ) modeling system to build a national air quality forecasting system, Weather Forecast., 20, 367–384, 2005. 4911
Palmer, P., Jacob, D., Fiore, A., Martin, R., Chance, K., and Kurosu, T.: Mapping isoprene emissions over North America using formaldehyde column observations from space, J. Geophys. Res.-Atmos., 108, 4180, doi:10.1029/2002JD002153, 2003. 4942, 4943
Palmer, P. I., Abbot, D. S., Fu, T.-M., Jacob, D. J., Chance, K., Kurosu, T. P., Guenther, A., Wiedinmyer, C., Stanton, J. C., Pilling, M. J., Pressley, S. N., Lamb, B., and Sumner, A. L.: Quantifying the seasonal and interannual variability of North American isoprene emissions using satellite observations of the formaldehyde column, J. Geophys. Res.-Atmos., 111, D12315, doi:10.1029/2005JD006689, 2006. 4942, 4943
Parrington, M., Jones, D. B. A., Bowman, K. W., Thompson, A. M., Tarasick, D. W., Merrill, J., Oltmans, S. J., Leblanc, T., Witte, J. C., and Millet, D. B.: Impact of the assimilation of ozone from the tropospheric emission spectrometer on surface ozone across North America, Geophys. Res. Lett., 36, L04802, doi:10.1029/2008GL036935, 2009. 4913
Pierce, R. B., Schaack, T., Al-Saadi, J. A., Fairlie, T. D., Kittaka, C., Lingenfelser, G., Natarajan, M., Olson, J., Soja, A., Zapotocny, T., Lenzen, A., Stobie, J., Johnson, D., Avery, M. A.,

ACPD
15, 4909–4971, 2015

Sachse, G. W., Thompson, A., Cohen, R., Dibb, J. E., Crawford, J., Rault, D., Martin, R., Szykman, J., and Fishman, J.: Chemical data assimilation estimates of continental US ozone and nitrogen budgets during the intercontinental chemical transport experiment – North America, J. Geophys. Res.-Atmos., 112, D12S21, doi:10.1029/2006JD007722, 2007. 4913

Pryor, W.: How far does ozone penetrate into the pulmonary air tissue boundary before it reacts, Free Radical Bio. Med., 12, 83–88, 1992. 4911

Rodgers, C. D.: Inverse Methods for Atmospheric Sounding – Theory and Practice, World Scientific, Singapore, 2000. 4917, 4926

Sandu, A., Daescu, D., and Carmichael, G.: Direct and adjoint sensitivity analysis of chemical kinetic systems with KPP: Part I – theory and software tools, Atmos. Environ., 37, 5083–5096, doi:10.1016/j.atmosenv.2003.08.019, 2003a. 4913

Sandu, A., Daescu, D., and Carmichael, G.: Direct and adjoint sensitivity analysis of chemical kinetic systems with KPP: Part I – theory and software tools, Atmos. Environ., 37, 5083–5096, doi:10.1016/j.atmosenv.2003.08.019, 2003b. 4918, 4922

Sillman, S.: Tropospheric ozone – the debate over control strategies, Annu. Rev. Energ. Env., 18, 31–56, doi:10.1146/annurev.energy.18.1.31, 1993. 4912, 4939

Stavrakou, T., Müller, J.-F., De Smedt, I., Van Roozendael, M., van der Werf, G. R., Giglio, L., and Guenther, A.: Global emissions of non-methane hydrocarbons deduced from SCIAMACHY formaldehyde columns through 2003–2006, Atmos. Chem. Phys., 9, 3663–3679, doi:10.5194/acp-9-3663-2009, 2009. 4942

Strunk, A., Ebel, A., Elbern, H., Friese, E., Goris, N., and Nieradzik, L. P.: Four-dimensional variational assimilation of atmospheric chemical data–application to regional modelling of air quality, in: Large-Scale Scientific Computing, 214–222, Springer, New York City, USA, 2010. 4912

Tawfik, A. B., Stoeckli, R., Goldstein, A., Pressley, S., and Steiner, A. L.: Quantifying the contribution of environmental factors to isoprene flux interannual variability, Atmos. Environ., 54, 216–224, doi:10.1016/j.atmosenv.2012.02.018, 2012. 4918

Tingey, D., Manning, M., Grothaus, L., and Burns, W.: Influence of light and temperature on isoprene emission rates from live oak, Physiologia Plantarum, 47, 112–118, doi:10.1111/j.1399-3054.1979.tb03200.x, 1979. 4918

Trainer, M., Williams, E., Parrish, D., Buhr, M., Allwine, E., Westberg, H., Fehsenfeld, F., and Liu, S.: Models and observations of the impact of natural hydrocarbons on rural ozone, Nature, 329, 705–707, doi:10.1038/329705a0, 1987. 4912

ACPD
15, 4909–4971, 2015

Valente, R., Imhoff, R., Tanner, R., Meagher, J., Daum, P., Hardesty, R., Banta, R., Alvarez, R., McNider, R., and Gillani, N.: Ozone production during an urban air stagnation episode over Nashville, Tennessee, J. Geophys. Res.-Atmos., 103, 22555–22568, 1998. 4916

Van Dingenen, R., Dentener, F. J., Raes, F., Krol, M. C., Emberson, L., and Cofala, J.: The global impact of ozone on agricultural crop yields under current and future air quality legislation, Atmos. Environ., 43, 604–618, doi:10.1016/j.atmosenv.2008.10.033, 2009. 4911

WHO: Review of evidence on health aspects of air pollution, Tech. rep., WHO (World Health Organization), Copenhagen, Denmark, 2013. 4911

Worden, H. M., Deeter, M. N., Edwards, D. P., Gille, J. C., Drummond, J. R., and Nedelec, P.: Observations of near-surface carbon monoxide from space using MOPITT multispectral retrievals, J. Geophys. Res.-Atmos., 115, D18314, doi:10.1029/2010JD014242, 2010. 4914

Worden, J., Liu, X., Bowman, K., Chance, K., Beer, R., Eldering, A., Gunson, M., and Worden, H.: Improved tropospheric ozone profile retrievals using OMI and TES radiances, Geophys. Res. Lett., 34, L01809, doi:10.1029/2006GL027806, 2007. 4914

Yi, J. and Prybutok, V.: A neural network model forecasting for prediction of daily maximum ozone concentration in an industrialized urban area, Environmental Pollut., 92, 349–357, 1996. 4911

Zhang, L., Constantinescu, E. M., Sandu, A., Tang, Y., Chai, T., Carmichael, G. R., Byun, D., and Olaguer, E.: An adjoint sensitivity analysis and 4D-Var data assimilation study of Texas air quality, Atmos. Environ., 42, 5787–5804, doi:10.1016/j.atmosenv.2008.03.048, 1st International Conference on Atmospheric Chemical Mechanisms, Univ Calif Davis, Davis, CA, 6–8 December 2006, 2008. 4911, 4912, 4913, 4917, 4939, 4942

Zhang, Y., Bocquet, M., Mallet, V., Seigneur, C., and Baklanov, A.: Real-time air quality forecasting, part II: State of the science, current research needs, and future prospects, Atmos. Environ., 60, 656–676, 2012. 4912

Zhu, C., Byrd, R., Lu, P., and Nocedal, J.: Algorithm 778: L-BFGS-B: Fortran subroutines for large-scale bound-constrained optimization, ACM T. Math. Software, 23, 550–560, 1997. 4922, 4933

Zoogman, P., Jacob, D. J., Chance, K., Zhang, L., Le Sager, P., Fiore, A. M., Eldering, A., Liu, X., Natraj, V., and Kulawik, S. S.: Ozone air quality measurement requirements for a geostationary satellite mission, Atmos. Environ., 45, 7143–7150, doi:10.1016/j.atmosenv.2011.05.058, 2011. 4914

ACPD
15, 4909–4971, 2015

Zoogman, P., Jacob, D. J., Chance, K., Liu, X., Lin, M., Fiore, A., and Travis, K.: Monitoring high-ozone events in the US Intermountain West using TEMPO geostationary satellite observations, Atmos. Chem. Phys., 14, 6261–6271, doi:10.5194/acp-14-6261-2014, 2014. 4914

ACPD
15, 4909–4971, 2015

Table 1. Background free tropospheric concentrations of trace gases mixed into the boundary layer in the photochemical model.

Chemical Species	Background Mixing Ratio
Ozone	30 ppbv
NO	100 pptv
NO_2	50 pptv
CO	80 ppbv
CH_4	1.76 ppm
NMHCs	100–200 pptv each

ACPD
15, 4909–4971, 2015

Table 2. Values of $\overline{F(\boldsymbol{x})}$ used to calculate $\boldsymbol{y}$. The overbar indicates that this represents the mean value.

$F(\hat{\boldsymbol{x}})$	Mixing Ratio
Ozone	44.4 ppbv
CO	620 ppbv
NO_2	6.5 ppbv
HCHO	3.9 ppbv

ACPD
15, 4909–4971, 2015

Table 3. Values of x and x_a used in the 4-D-variational data assimilation model.

x			x_a		
NO	CO	VOC	NO	CO	VOC
0.5	1.0	6.5	0.475	0.95	0.1
0.75	–	–	0.7125	–	–
1.0	–	–	0.95	–	–
1.25	–	–	1.1875	–	–
1.5	–	–	1.425	–	–
1.75	–	–	1.8375	–	–
2.0	–	–	2.1	–	–
2.25	–	–	2.3625	–	–
2.5	–	–	2.625	–	–

ACPD
15, 4909–4971, 2015

Table 4. Initial peak ozone predictions, true state peak ozone, initial guess ozone prediction error, and prediction error across the full range of x_{NO} and the three observing scenarios CN, OCN and HCN. The ozone values and absolute differences in ozone mixing ratio are listed for 3 p.m. during the final day of the prediction model. Figure 3 shows what E and G represent.

x_{NO} Scenario	$q_{O_3}(\boldsymbol{x}_a, t^{\mu})$ (ppbv)	$q_{O_3}(\boldsymbol{x}, t^{\mu})$ (ppbv)	G (ppbv)	E (ppbv) Scenario CN	E (ppbv) Scenario OCN	E (ppbv) Scenario HCN
0.5	72.7	79.3	−6.6	−6.3	−0.4	−1.0
0.75	81.3	89.7	−8.4	−8.3	−0.5	−0.7
1.0	85.2	96.3	−11.1	−4.5	−0.6	−0.5
1.25	85.5	100.3	−15.1	−3.3	−0.6	−0.3
1.5	79.7	101.5	−21.8	−4.2	−0.5	−0.1
1.75	66.1	98.7	−32.6	2.2	0.3	0.2
2.0	52.8	89.0	−36.2	1.9	0.3	0.2
2.25	43.6	73.0	−29.4	1.4	0.3	0.2
2.5	37.1	58.8	−21.7	1.0	0.3	0.2

ACPD
15, 4909–4971, 2015

Table 5. The a posteriori x_{VOC} error resulting from the 4-D-variational data assimilation. The table shows the variability of the a posteriori VOC emission error both with observing scenario and NO emission factor. Errors are represented as absolute errors of x_{VOC}.

x_{NO}	$\hat{x}_{VOC} - x_{VOC}$ Scenario CN	Scenario OCN	Scenario HCN
0.5	−6.4	0.40	8.5×10^{-2}
0.75	9.1	0.33	5.0×10^{-2}
1.0	−2.7	−0.01	3.3×10^{-2}
1.25	−1.6	9.87	-2.6×10^{-2}
1.5	−1.7	2.71	-3.6×10^{-2}
1.75	0.77	0.21	2.4×10^{-2}
2.0	0.54	0.20	3.3×10^{-2}
2.25	0.40	0.18	4.5×10^{-2}
2.5	0.35	0.18	4.8×10^{-2}

ACPD
15, 4909–4971, 2015

Table 6. Results from a study exploring the sensitivity of the 4-D-variational data assimilation forecast of peak ozone to varying assumptions regarding, $k(t)$, the diurnal variability of ozone precursor emissions. Note that in each scenario the cumulative daily emission burden remains constant for each scenario and thus each scenario has identical $\overline{E(t)}$. The overbar indicates that this represents the mean value. The table shows (in ppbv) the modeled ozone for each alternative $k(t)$ scenario, the differences in true state peak ozone between these alternative $k(t)$ scenarios and the standard $k(t)$ scenario, and the absolute a posteriori ozone prediction errors of these alternative $k(t)$ scenarios relative to both the standard and alternative $k(t)$ scenario true states. All of the ozone mixing ratios are listed for 3 p.m. during the final day of the prediction and monitoring period.

Assumed $k(t)$ Scenario	Alternative Emission Scenario (ppbv)	Alternative Emission Scenario True State – Standard Emission Scenario True State (ppbv)	Alternative Ozone Prediction Error – Standard True State (ppbv)	Alternative Ozone Prediction Error – Alternative True State (ppbv)
Constant	92.5	2.8	4.0	0.7
Sine Wave	97.6	7.9	8.8	0.5
Saw-Tooth	100.3	10.6	9.7	−1.4
Offset −1	93.8	4.2	4.7	0.1
Offset −2	98.9	9.0	9.2	−0.2
Offset +1	86.2	−3.5	−4.9	−1.4
Offset +2	83.5	−6.2	−8.6	−2.4

ACPD
15, 4909–4971, 2015

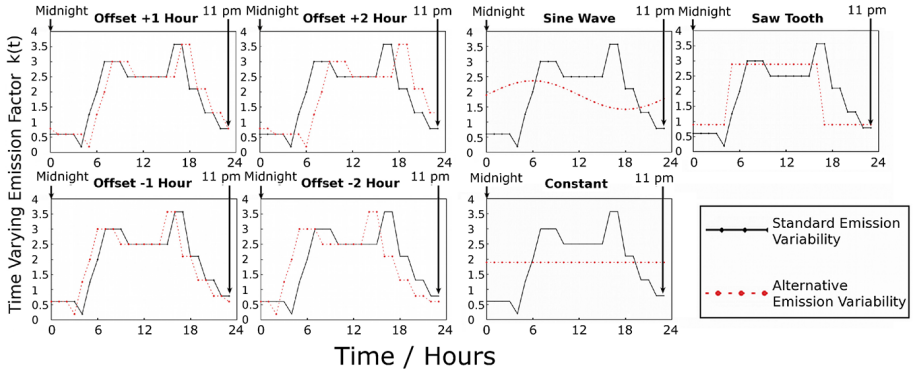

Figure 1. The various different profiles of the temporal variability emission factor, $k(t)$, used in the analysis of the emission solution sensitivity to diurnal emission variability. The red dashed and the solid black lines indicate the alternative and standard emissions variabilities, respectively. The different profiles of variability are indicated at the top of each panel in bold text.

ACPD
15, 4909–4971, 2015

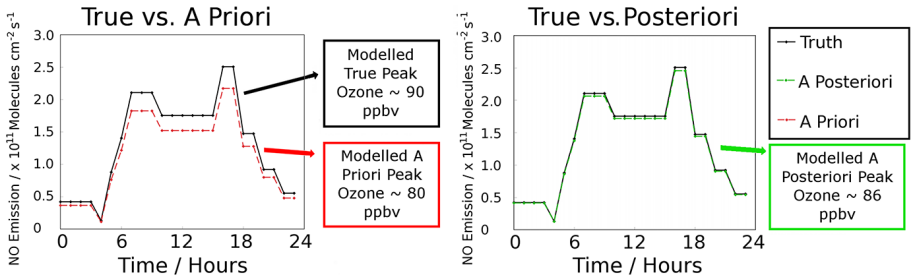

Figure 2. A schematic showing how both the a priori and a posteriori emissions relate to the true emissions of NO, and the modeled peak afternoon ozone that results from these emission variabilities. Note that the same emission variability is used for all of the anthropogenic chemical species emitted in the model. The a priori and a posteriori emissions are scaled relative to the true emissions and these differences can be characterized as being due to different emission scaling factors (i.e., x_{NO}) for the a priori, a posteriori and true emissions. The black solid, green dashed and red dashed lines show the truth, a posteriori, and a priori emissions, respectively.

ACPD
15, 4909–4971, 2015

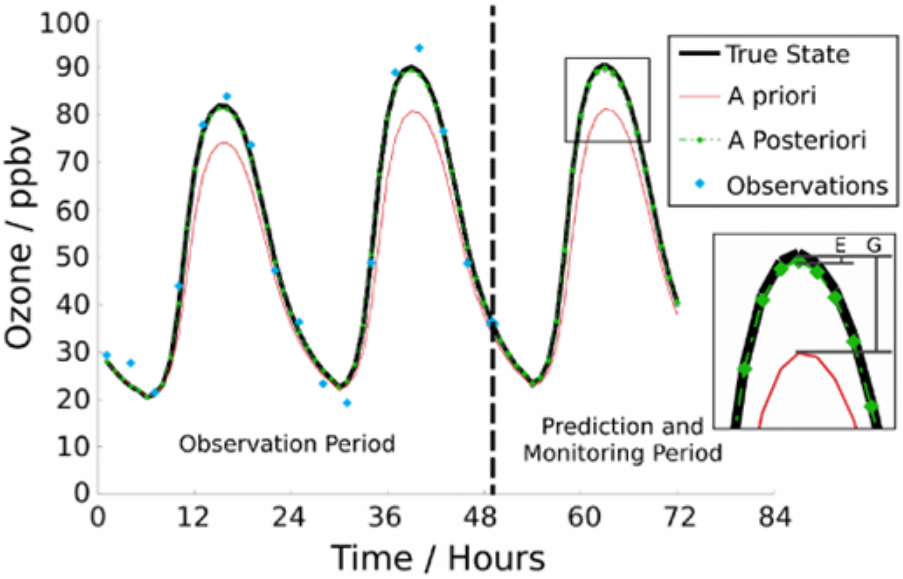

Figure 3. A representation of the ozone prototype forecasting framework and the 4-D-variational data assimilation results for scenario OCN with $\beta = 0.1$. The observation period covers the first 48 h period of the assimilation during which time pseudo observations are made (at a frequency of every 3 h in this case) and are used within the assimilation. The observations are used to constrain the emissions of ozone precursors, which in turn allows the forecasting model to produce the a posteriori ozone prediction. During the prediction and monitoring period the model true state now plays the monitoring role allowing comparisons to be made to the ozone forecast. The a posteriori ozone prediction represents the forecast for ozone concentrations one day in the future. E represents the a posteriori prediction model error and G represents the a priori and intitial guess prediction error. The black solid line, red solid line, green dashed line, and blue diamonds represent the truth, a priori, a posteriori, and pseudo observations, respectively.

ACPD
15, 4909–4971, 2015

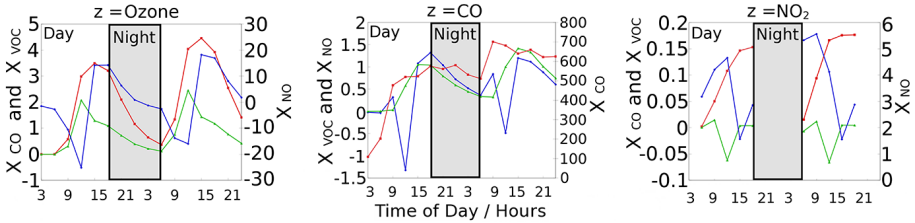

Figure 4. These plots show the columns of the Jacobian matrix, **K**, that correspond to the perturbations of the three observed species in scenario OCN. Ozone is shown on the left, CO in the middle, and NO_2 on the right. This Jacobian is for the x_{NO} = 1.25 emission scenario. The shaded area represents observations made during the night. NO_2 observations made using visible remote sensing instruments can only function during the daytime, so there is no need to include a row in the Jacobian corresponding to night time NO_2 observations. The blue, green, and red solid lines represent $q_Z(\boldsymbol{x},t)/\partial x_{NO}$, $q_Z(\boldsymbol{x},t)/\partial x_{NO}$, and $q_Z(\boldsymbol{x},t)/\partial x_{NO}$, respectively. The y axes on the left and right represent the different perturbations to x.

ACPD
15, 4909–4971, 2015

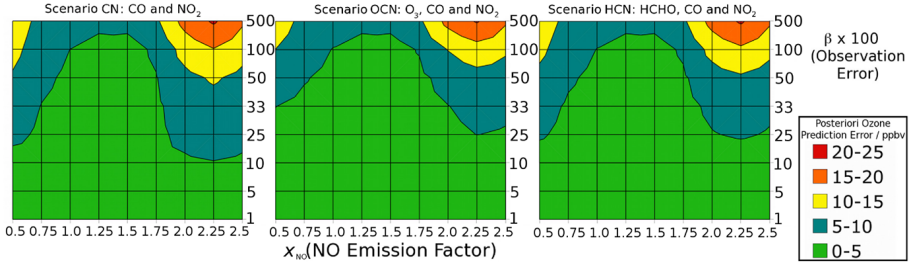

Figure 5. Ozone a posteriori prediction errors across the complete range of parameter space for x_{NO} (0.5–2.5) on the x axis and β (0.1–5) along the y axis with each panel presenting the results from the three observing scenarios CN, OCN and HCN. The colored contours represent the a posteriori prediction error in units of ppbv. The green and red colors indicate low and high levels of a posteriori ozone prediction error, respectively.

ACPD
15, 4909–4971, 2015

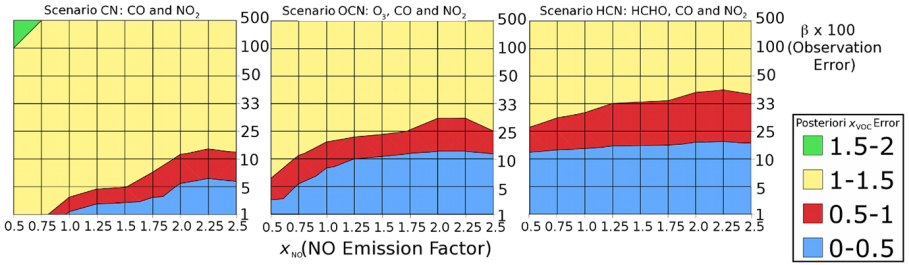

Figure 6. x_{VOC} a posteriori errors across the complete range of parameter space for x_{NO} (0.5–2.5) on the x axis and β (0.1–5) along the y axis with each panel presenting the results from the three observing scenarios **(a–c)**. The colored contours represent the a posteriori error. To allow comparison of the error in x_{VOC} to the true state we note that the true state is defined as x_{VOC} = 6.5. The light blue and green colors indicate low and high a posteriori error on x_{VOC}, respectively.

ACPD
15, 4909–4971, 2015

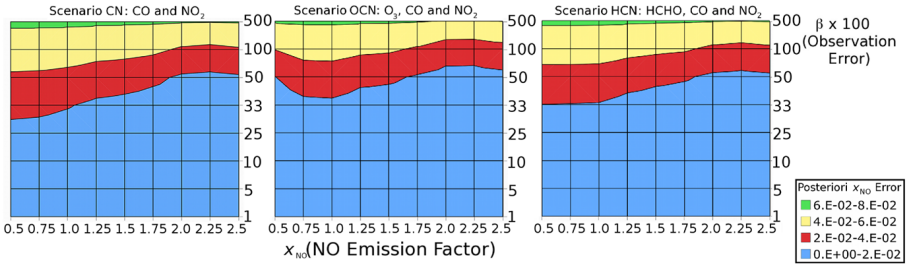

Figure 7. x_{NO} a posteriori errors across the complete range of parameter space for x_{NO} (0.5–2.5) on the x axis and β (0.1–5) along the y axis with each panel presenting the results from the three observing scenarios CN, OCN and HCN. The colored contours represent the a posteriori error. To allow comparison of the error in x_{NO} to the true state we note that the true state is defined as the x axis value. The light blue and green colors indicate low and high a posteriori error on x_{NO}, respectively.

ACPD
15, 4909–4971, 2015

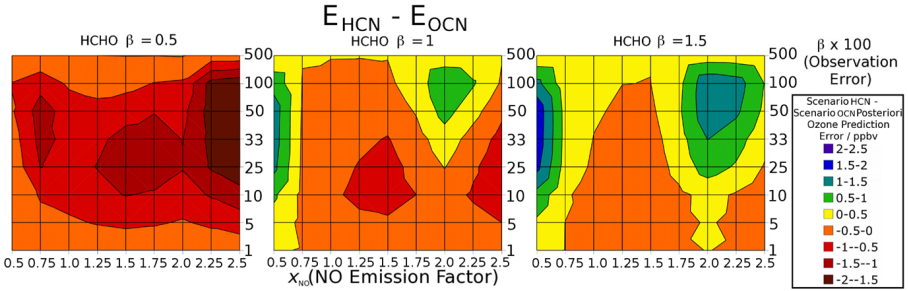

Figure 8. The difference between the scenario HCN and OCN a posteriori ozone prediction error for a range of assumed HCHO observing error scenarios. In all of the previous analyses and results β has been identical for all observed species, but in this sensitivity analysis we scale β for HCHO independently from the other observed species. From left to right HCHO observing errors are assumed to be 50, 100, and 150 % of the observing error for the other species. Thus the right hand panel indicates a scenario with HCHO observations to be of poorer quality relative to the other species, and represents the difference in ozone prediction error between the right and middle panels of Fig. 5, and the left panel indicates a rather optimistic case with assumed HCHO observation errors to be less than the other observed species errors. The brown and purple contour colors indicate the negative and positive differences between the scenario HCN and OCN a posteriori ozone prediction error, respectively.

ACPD
15, 4909–4971, 2015

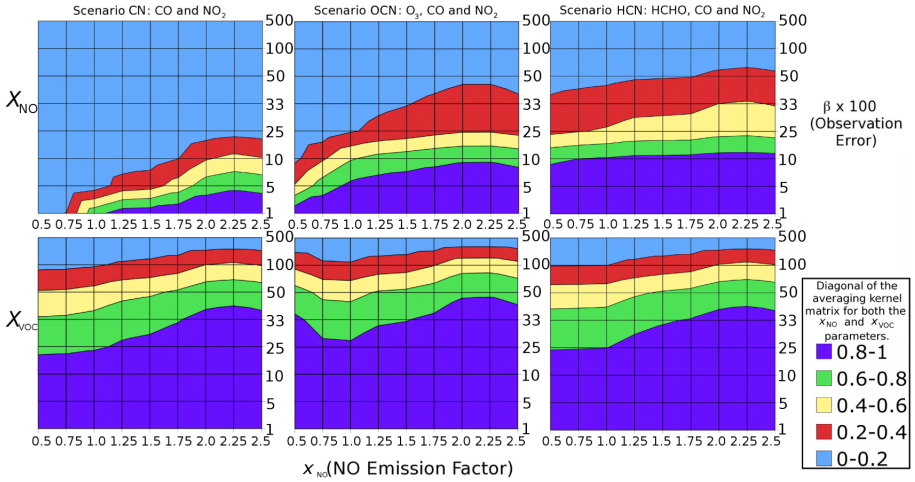

Figure 9. The diagonal of the averaging kernel for x_{VOC} on the lower row and x_{NO} on the upper row. Each column represents a different observing scenario (CN, OCN, and HCN). The x axis denotes the varying value of x_{NO} and the y axis shows β (0.1–5). The contours represent the varying magnitude of the diagonal of the averaging kernel matrix from 0 to 1. The purple and light blue contour colors indicate high and low values of the diagonal of the averaging kernel matrix, respectively.

ACPD
15, 4909–4971, 2015

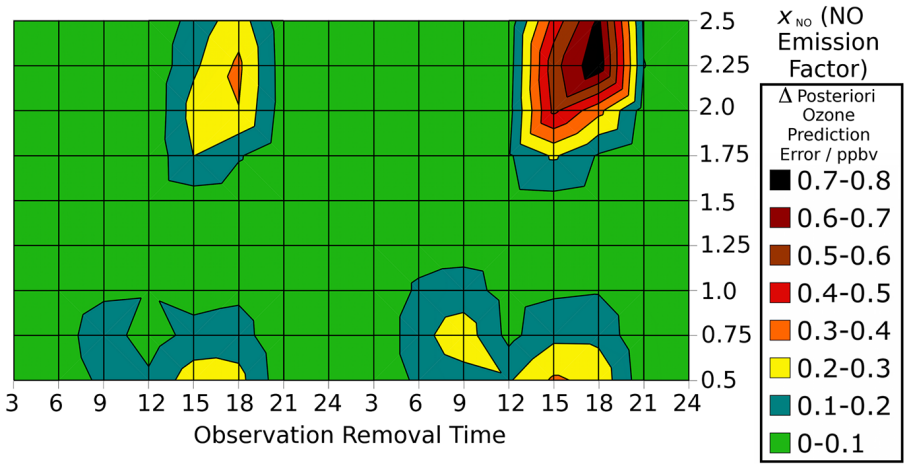

Figure 10. The absolute increase in a posteriori ozone prediction error between scenario OCN with $\beta = 0.25$ and the same scenario with observations removed form specific times over the course of 2 days (perturbed case), e.g., hour 15 on the second day indicates that no observations were included in the analytical model calculation of a posteriori ozone prediction error for the perturbed case from 3 p.m. on the second day. The green and black colors indicate low and high values, respectively.

ACPD
15, 4909–4971, 2015

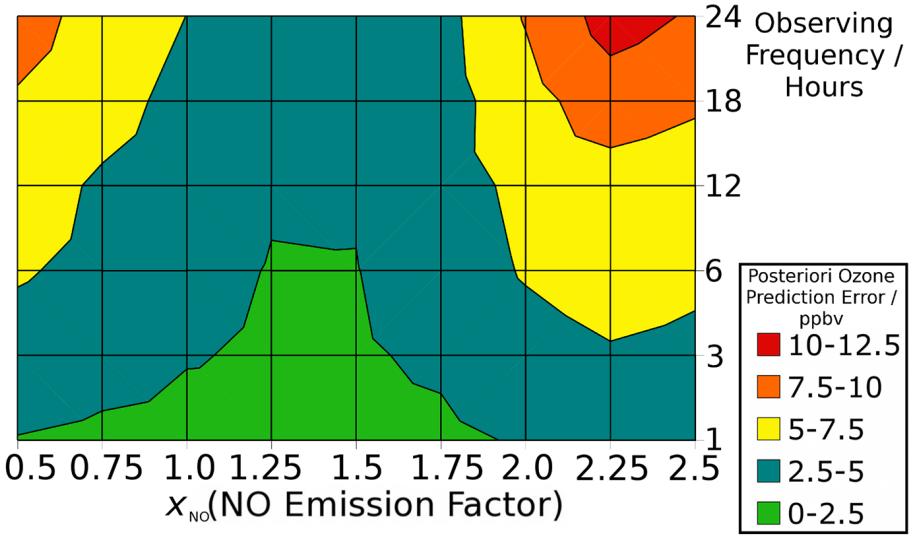

Figure 11. The a posteriori ozone prediction error for a variety of observation frequency scenarios ranging from an observing frequency of 1 h to once per day. These were calculated for scenario OCN with β = 0.25. The green and red colors indicate low and high levels of a posteriori ozone prediction error, respectively.

ACPD
15, 4909–4971, 2015

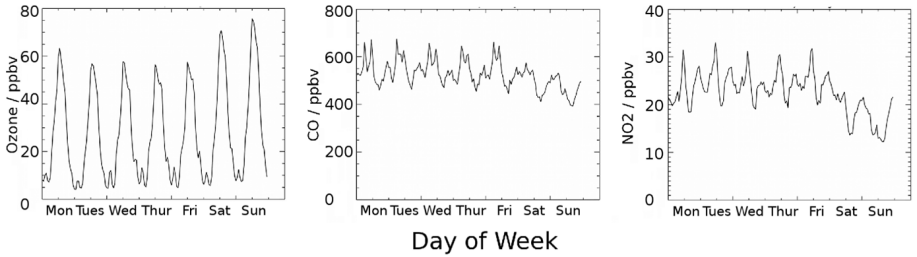

Figure 12. Weekly averaged late summer and early fall ozone, CO, and NO_2 variability. Data from the months July, August and September and years 2005 though to 2008 are included in the analysis to create the average weekly variability. These results show persistent pattern of day to day variability for these trace gases related to the specific day of the week. The plots on the left, center, and right show the ozone, CO, and NO_2 mixing ratios, respectively.

ACPD
15, 4909–4971, 2015